Ph.D. Thesis Dissertation

Experimental estimation of soil emissivity and its application to soil moisture retrieval in the SMOS mission

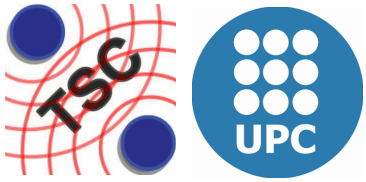

Alessandra Monerris i Belda

Remote Sensing Laboratory
Dept. Teoria del Senyal i Comunicacions
Universitat Politècnica de Catalunya

Ph.D. Thesis advisors

Dr. Adriano J. Camps Carmona & Dr. Mercè Vall-llossera Ferran

Barcelona, June 2009

Chapter 8

Topography impact on ground-based radiometric measurements

Since the Earth's surface is not flat, the retrieval of geophysical variables from satellite data must account for topography effects on the measurements. Moreover, topography affects the distribution of soil moisture, which accumulates at the valleys, and decreases at elevated peak zones. The topography issue may be important in the case of SMOS since, considering the size of a SMOS pixel which can be on average 50 km $\times$ 50 km, there is a high probability of having pixels within a footprint which are affected by topography.

In this chapter, ground-based measurements at L-band of a valley acquired using the LAURA radiometer have been compared to simulated antenna temperatures to assess the impact of topography. Four different scenarios have been simulated: (i) an hypothetical flat scenario without vegetation, (ii) an hypothetical flat scenario with the actual land cover map of the experiment site, (iii) an hypothetical scenario without vegetation but with the digital elevation map of the experiment site, and (iv) the actual experiment site, including both the digital elevation model and the land cover map.

8.1 Introduction

Few airbone radiometric data at L-band are available to address the issue of topography effects on brightness temperature [Berger *et al.*, 2002, Walker & Panciera, 2005]. Thus, most of the existing studies have attempted to characterise with models the topographic effects on passive microwave measurements from satellite.

The first attempt to estimate the topography impact from simulated data was done by Mätlzler & Standley [2000], who noted not only changes in the local incidence angle, but also shadowing effects, and a variable contribution of the atmosphere as a function of altitude. These effects were also observed in studies by Talone *et al.* [2007] and Kerr *et al.* [2003]. Pierdicca *et al.* [2008] noted an overestimation of the brightness temperature at horizontal polarisation

with respect to that of a flat terrain, whereas both under and overestimation occurred at vertical polarisation. In Zurita [2008], data from the CoSMOS-Aus field experiment were analysed [Walker & Panciera, 2005]. Errors in brightness temperature up to 5 K were estimated if topography was neglected, and it was noted that polarisation mixing introduced a bias in the simulations greater than 3 K, and had a larger impact at nadir.

These perturbing effects above may lead to a wrong estimation of soil moisture, having uncertainties higher than SMOS 4% requirements [Barré *et al.*, 2008]. SMOS soil moisture retrieval level 2 algorithm does not allow taking into account topography perturbations since computational requirements would be too high. So, retrieval algorithms are designed for flat surfaces, and pixels are flagged as flat, moderate topography, and strong topography [Coret *et al.*, 2006, Mialon *et al.*, 2008]. The last category precludes any soil moisture retrieval at the SMOS scale.

Next sections describe the results of the Topography effects on RadiomeTry at L-band Experiment (TuRTLE), conducted during two weeks in Spring 2006 [Monerris *et al.*, 2008, Benedicto, 2007]. TuRTLE 2006 is a study of the topography issue from a ground-based radiometer, so the atmospheric contribution in this case is negligible. However, topography impact on the local incidence angle and polarisation mixing was observed and is presented hereafter.

8.2 TuRTLE 2006 experiment overview

The Topography effects on RadiomeTry at L-band Experiment (TuRTLE) 2006 was carried out at the Parc Natural del Montseny, Barcelona, Spain (41°48′ N, 2°19′ E; Fig. 8.1(a)). The LAURA radiometer was installed at 898 m altitude looking at a valley so that, as the antenna moved in azimuth and elevation, observations of the descending and ascending mountain slopes, as well as of the transition between the mountain peak and the sky could be done.

A two-dimensional digital elevation map and a land cover map of the site are represented in Fig. 8.1(b) and Fig. 8.1(c), respectively. In both figures, the position of LAURA is indicated with a black circle. The site is mainly covered by mixed woodland, and to a minor extent of shrubs, crops, and bare areas as can be seen from the land cover map of the area in Fig. 8.1(c). The numerical coding of each cover type is indicated in Table 8.1. Scans in azimuth covered the area between lines labelled as $\varphi_A = 130°$ and $\varphi_A = 50°$ in the plots. On the other hand, the

Table 8.1: Land cover types at the TuRTLE 2006 experiment site. Values for the land cover map reference and single scattering albedo, b-parameter, and vegetation water content (VWC) used as inputs to the antenna brightness temperature simulator are presented.

Vegetation Type	land cover #	ω	b	VWC ($\mathrm{kg \cdot m^2}$)
Mixed woodland	1–3	0.12	0.20	2
Shrub	7	0.12	0.20	0.3
Crop/mixed farming	17	0.05	0.13	0.5
Bare	13	-	-	-

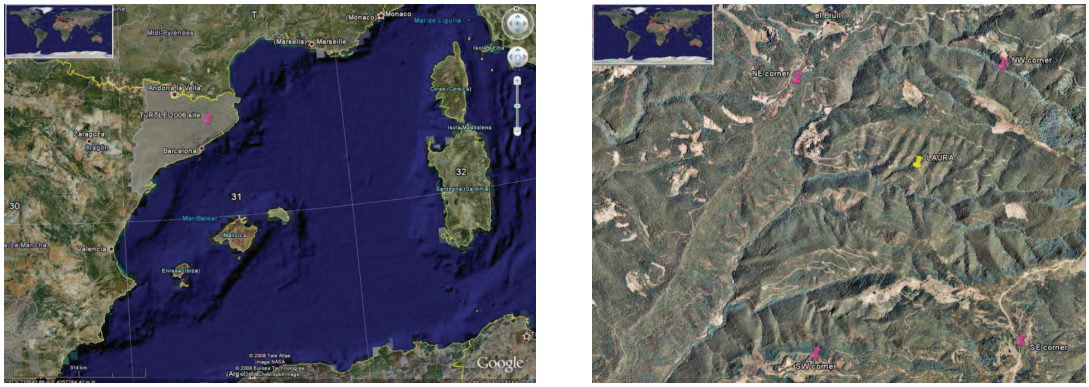

(a)

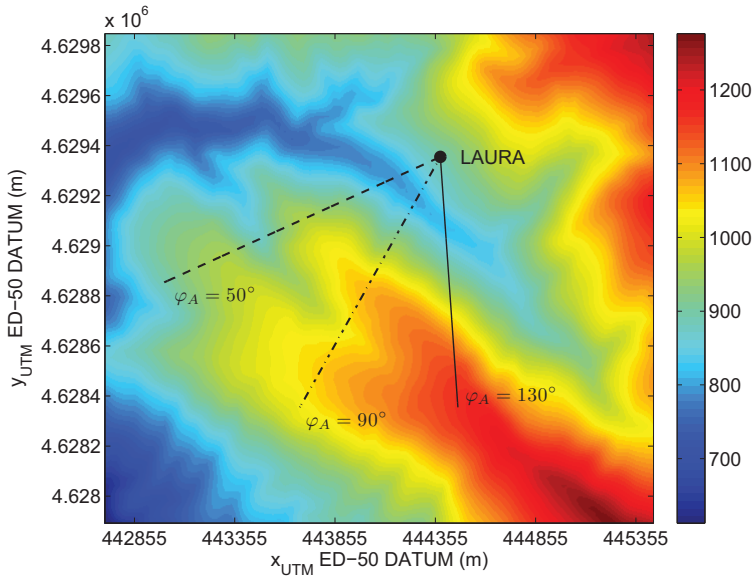

(b)

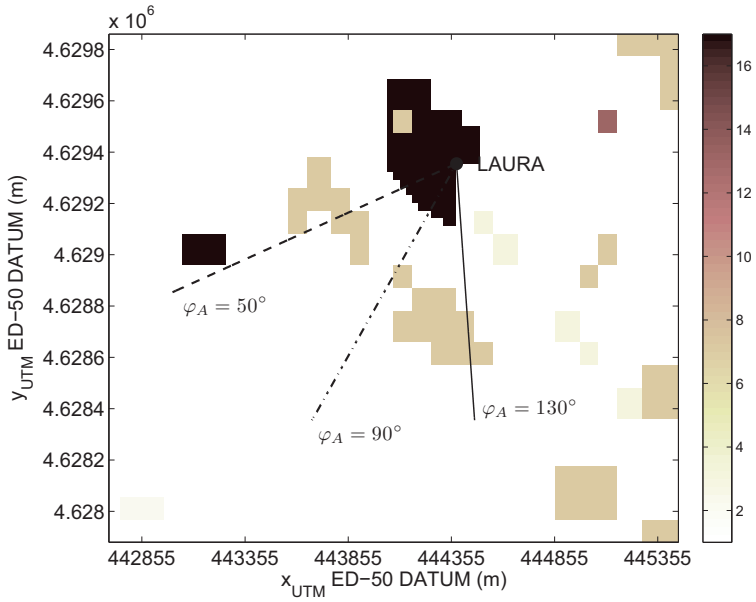

(c)

Fig. 8.1: Overview of the TuRTLE 2006 experiment site. (a) Google-Earth image. (b) Two-dimensional digital elevation map. (c) Land cover map (see Table 8.1 for numerical coding of the land cover type). In (b) and (c) the position of the LAURA radiometer is indicated with a black circle. Lines indicate the direction of observation for the three azimuth angles: $\varphi_A = 130°$, $\varphi_A = 90°$, and $\varphi_A = 50°$.

antenna elevation angle with respect to nadir varied from 45° to 105°. Further information on this experiment is given in Chapter 4, Section 4.8.

8.3 Simulation of the antenna temperature

Antenna brightness temperature was simulated for each pixel in order to compare model results to LAURA collected measurements. The antenna brightness temperature at each observation position was simulated using a 30 m resolution digital elevation model (DEM) [de Catalunya, 2004], and a 100 m resolution land cover map of the site [CREAF, 2006]. The cover map was interpolated to obtain a 30 m resolution grid, as the DEM, since this was the reference grid of the simulator. A geometric surface facet model was used to estimate the local incidence angle and the polarisation mixing due to surface tilting at each observation position. Next sections describe the formulation employed in the antenna temperature simulator.

8.3.1 Global coordinate system

The universal transverse mercator (UTM) ED50 coordinates have been selected as the global coordinate system in the antenna brightness temperature simulator. The digital elevation map was already referred to this system [de Catalunya, 2004], but the positions of the radiometer and the observed pixel had to be converted to UTM ED50 coordinates. Figure 8.2 shows the definition of the direction vector $\hat{k}$ from the radiometer to the observed pixel, which can be expressed in the antenna coordinate system as $\hat{k} = -(\sin\theta_A \cos\varphi_A, \sin\theta_A \sin\varphi_A, \cos\theta_A)$. The matrix

$$\bar{\bar{\Lambda}} = \begin{pmatrix} -\cos\theta_A \cos\gamma & -\sin\gamma & -\sin\theta_A \cos\gamma \\ -\cos\theta_A \sin\gamma & \cos\gamma & -\sin\theta_A \sin\gamma \\ \sin\theta_A & 0 & -\cos\theta_A \end{pmatrix} \tag{8.1}$$

has been used to shift coordinates between the antenna and the global coordinate system. The variable γ is defined as

$$\gamma = \varphi_o - \alpha_A - \varphi_A, \tag{8.2}$$

where $\varphi_o = 60°$ is the relative angle between the radiometer trailer's orientation and the geographic North, and $\alpha_A = 0.4452°$ is the UTM meridian convergence of the radiometer position.

Once the conversion matrix has been obtained, the coordinates of the direction vector $\hat{k}^{\mathrm{UTM}}$ and the polarization vectors $\hat{v}_A^{\mathrm{UTM}}$ and $\hat{h}_A^{\mathrm{UTM}}$ in the global coordinate system are estimated as

$$\begin{aligned} \hat{k}^{\mathrm{UTM}} &= \bar{\bar{\Lambda}} \cdot \hat{k}, \\ \hat{v}_A^{\mathrm{UTM}} &= \bar{\bar{\Lambda}} \cdot \hat{v}_A, \\ \hat{h}_A^{\mathrm{UTM}} &= \bar{\bar{\Lambda}} \cdot \hat{h}_A, \end{aligned} \tag{8.3}$$

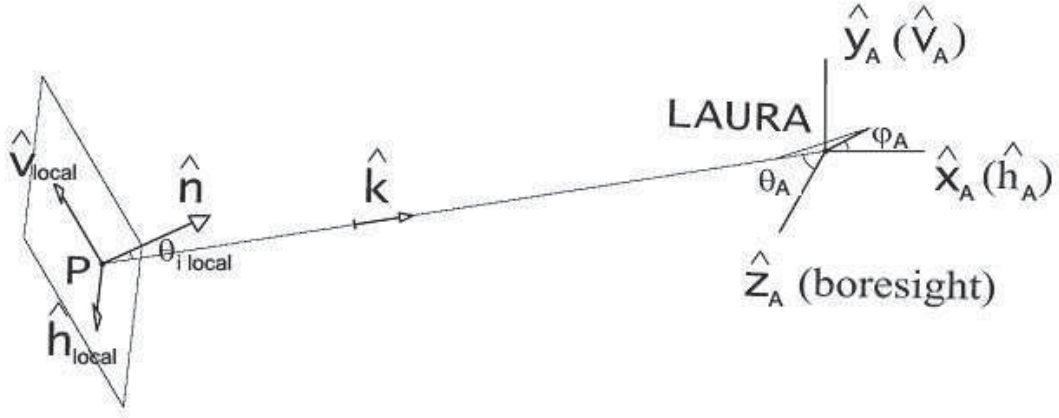

Fig. 8.2: Geometry problem in TuRTLE. The direction vector $\hat{k}$ corresponds to the observed pixel's direction within the antenna pattern, P is the position of the pixel, and θ_{local} is the local incidence angle. The direction vector $\hat{k}$ is referred to the antenna coordinate system by the angles θ_A and φ_A.

where $\hat{v}_A = \hat{y}_A = (0, 1, 0)$, and $\hat{h}_A = \hat{x}_A = (1, 0, 0)$, and the superscript UTM indicates that the parameters are referenced to the UTM ED50 coordinate system.

8.3.2 Determination of the pixels under observation

The pixel over the surface viewed by the radiometer changes with the antenna angles (θ_A, φ_A). This pixel has an associated unitary normal vector $\hat{n}^{\text{UTM}}$, from which the local incidence angle θ_{local}, and polarisation vectors $\hat{v}_{\text{local}}^{\text{UTM}}$ and $\hat{h}_{\text{local}}^{\text{UTM}}$ can be estimated. This situation is represented in Fig. 8.2. In the antenna brightness temperature simulator, the position of the observed pixel is estimated by finding the intersection of the line that passes through the radiometer coordinates and has the direction vector $\hat{k}^{\text{UTM}}$, with the digital elevation model. The parametric equation of this line can be written as

$$\vec{P}^{\text{UTM}} = a \cdot \hat{k}^{\text{UTM}} + \vec{P}_{\text{LAURA}}^{\text{UTM}}, \tag{8.4}$$

where $\vec{P}^{\text{UTM}}$ is the position vector of the pixel, a is a variable ranging from $-\infty$ to ∞, $\hat{k}^{\text{UTM}}$ is the unit vector of the antenna pattern estimated in (8.4), and $\vec{P}_{\text{LAURA}}^{\text{UTM}}$ is the position vector of the radiometer, all expressed in global coordinates.

8.3.3 Estimation of the local incidence angle

In an hypothetical no-topography scenario, the local incidence angle θ_{local} is equal to the antenna elevation angle θ_A. However, when topography is not negligible, the local incidence angle is different from the antenna elevation angle and θ_{local} has to be estimated as

$$\theta_{\text{local}} = \arccos\left(\hat{k}^{\text{UTM}} \cdot \hat{n}^{\text{UTM}}\right), \tag{8.5}$$

for every pixel observed at a position (θ_A, φ_A), where $\hat{n}^{\text{UTM}}$ is the vector normal to the soil surface at point $\vec{P}^{\text{UTM}}$ (see Fig. 78.2). It is important to note that, in this case, small

antenna elevation angles measured from nadir correspond to large local incidence angles θ_{local} and vice-versa.

8.3.4 Polarisation mixing

The antenna brightness temperature polarisation vectors at a pixel, $\vec{v}_{\text{local}}^{\text{UTM}}$ and $\vec{h}_{\text{local}}^{\text{UTM}}$, usually differ from those in the antenna reference system, $\vec{v}_A^{\text{UTM}}$ and $\vec{h}_A^{\text{UTM}}$, due to the polarisation mixing. If the polarisation vectors referred to the observed pixel are

$$\begin{aligned} \vec{h}_{\text{local}}^{\text{UTM}} &= \vec{k}^{\text{UTM}} \times \vec{n}^{\text{UTM}}, \\ \vec{v}_{\text{local}}^{\text{UTM}} &= \vec{h}_{\text{local}}^{\text{UTM}} \times \vec{k}^{\text{UTM}}, \end{aligned} \tag{8.6}$$

then, the electric fields in (θ_A, φ_A) are computed from (8.6) and the electric fields at the pixel, E_h^{local} and E_v^{local} as [Claassen & Fung, 1974]

$$\begin{pmatrix} E_\theta \\ \\ E_\varphi \end{pmatrix} = \begin{pmatrix} \hat{h}_{\text{local}}^{\text{UTM}} \cdot \hat{h}_A^{\text{UTM}} & \hat{v}_{\text{local}}^{\text{UTM}} \cdot \hat{h}_A^{\text{UTM}} \\ \\ \hat{h}_{\text{local}}^{\text{UTM}} \cdot \hat{v}_A^{\text{UTM}} & \hat{v}_{\text{local}}^{\text{UTM}} \cdot \hat{v}_A^{\text{UTM}} \end{pmatrix} \begin{pmatrix} E_h^{\text{local}} \\ \\ E_v^{\text{local}} \end{pmatrix}, \tag{8.7}$$

and, converting to the antenna reference frame,

$$\begin{pmatrix} E_x \\ E_y \end{pmatrix} = \begin{pmatrix} \cos\varphi_A & -\sin\varphi_A \\ \sin\varphi_A & \cos\varphi_A \end{pmatrix} \begin{pmatrix} E_\theta \\ E_\varphi \end{pmatrix}. \tag{8.8}$$

Then, the antenna brightness temperatures in the antenna reference frame, T_x and T_y, may be estimated from the electric fields, since $T_x \propto \langle |E_x|^2 \rangle$ and $T_y \propto \langle |E_y|^2 \rangle$.

8.3.5 Apparent temperature of the experiment site

The apparent temperature of a land cover observed by a downward-looking radiometer placed at a height H about the terrain can be expressed, according to Ulaby *et al.* [1981, p. 222], as

$$T_{AP}^{\text{model}}(\theta_A, \varphi_A; H; p) = T_{UP}(\theta_A; H) + \frac{1}{L_a(\theta_A; H)}[T_B^{\text{model}}(\theta_A, \varphi_A; p) + T_{SC}(\theta_A, \varphi_A; p)], \tag{8.9}$$

where $(\theta_A,\ \varphi_A)$ is the direction of observation, T_{UP} is the atmospheric upwelling emission, $T_B^{\text{model}}(\theta_A, \varphi_A; p)$ is the simulated brightness temperature of the observed pixel, T_{SC} is the atmospheric downward radiation scattered by the terrain in the direction of observation, $L_a(\theta_A; H)$ is the atmospheric loss factor, and p is the polarization (horizontal or vertical). The galactic terms were computed from numerical models that include the antenna orientation and pattern, its geographical coordinates, the date and time of measurements, atmospheric parameters, and the galactic noise map at 1420 MHz [Reich & Reich, 1986]. Since the experiment was ground-based,

the atmospheric attenuation was negligible ($L_a = 1$), and T_{UP} was close to 0 K. Taking this into account, the expression in (8.9) can be rewritten as

$$T_{AP}^{\text{model}}(\theta_A, \varphi_A; p) = T_B^{\text{model}}(\theta_A, \varphi_A; p) + T_{SC}(\theta_A, \varphi_A; p). \tag{8.10}$$

The brightness temperature $T_B^{\text{model}}(\theta_A, \varphi_A; p)$ was estimated for the observed pixel at (θ_A, φ_A) as in (3.26) [Ulaby *et al.*, 1986, p. 888]. Soil reflectivity was estimated from the soil dielectric constant [Wang & Schmugge, 1980], the local incidence angle θ_{local}, soil roughness, and the specular Fresnel reflectivity [Wang & Choudhury, 1981]. The atmospheric downward radiation (T_{DN}) scattered by the terrain was estimated as $T_{SC} = T_{DN}\Gamma^*_{\text{soil}}$. Input values used in simulations were estimated from measurements and from Zhan *et al.* [2006] taking into account the land cover map, and are listed in Table 8.1.

8.3.6 Integration over the antenna radiation pattern

Since LAURA's antenna beamwidth is finite, the antenna temperature T_A is estimated by integration of the apparent brightness temperature over the antenna radiation pattern. Neglecting the antenna cross-polar pattern, which is smaller than - 35 dB [Villarino, 2004, Camps *et al.*, 2004], and according to Ulaby *et al.* [1981, p. 204],

$$T_A^{\text{model}}(\theta_A, \varphi_A; p) = \frac{1}{\Omega_p} \iint\limits_{\text{antenna beam}} T_{AP}^{\text{model}}(\theta_A, \varphi_A; p) |F_{n_{pp}}(\theta_A, \varphi_A)|^2 d\Omega \tag{8.11}$$

where $T_{AP}^{\text{model}}(\theta_A, \varphi_A; p)$ is the apparent temperature in (8.10), $|F_{n_{pp}}(\theta_A, \varphi_A)|^2$ is the normalised antenna radiation pattern, Ω_p is the normalised antenna solid angle, and the subscript p indicates the polarisation (H or V).

8.4 Comparison between radiometric measurements and simulations

Four different scenarios have been simulated using the antenna brightness temperature described in the previous section. Although the experiment site was a mountainous area covered by vegetation on a large percentage, simulations have been carried out considering the following options: (i) an hypothetical scenario without vegetation and without topography, (ii) an hypothetical scenario without topography, but with the actual land cover map of the experiment site, (iii) an hypothetical scenario without vegetation, but with the digital elevation map of the experiment site, and (iv) the actual experiment site, including both the digital elevation model and the land cover map.

Measured and simulated antenna brightness temperatures are represented in Figs. 8.3(a) and 8.3(b) as a function of the antenna observation angle referred to nadir, θ_A. Solid lines indicate the radiometric measurements, and dashed and dash-dotted lines indicate simulations with bare soils (scenarios (i) and (iii)) and soil covered by vegetation (scenarios (ii) and (iv)) respectively, and icons denote the polarisation ($\square$ for H-polarisation, and $\star$ for V-polarisation). The solid vertical line depicted at $\theta_A = 90°$ indicates the antenna elevation angle corresponding

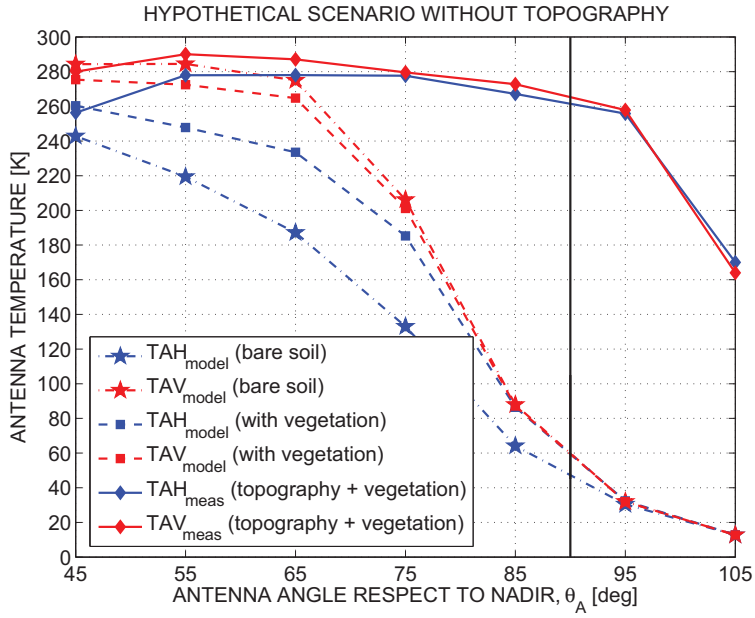

(a)

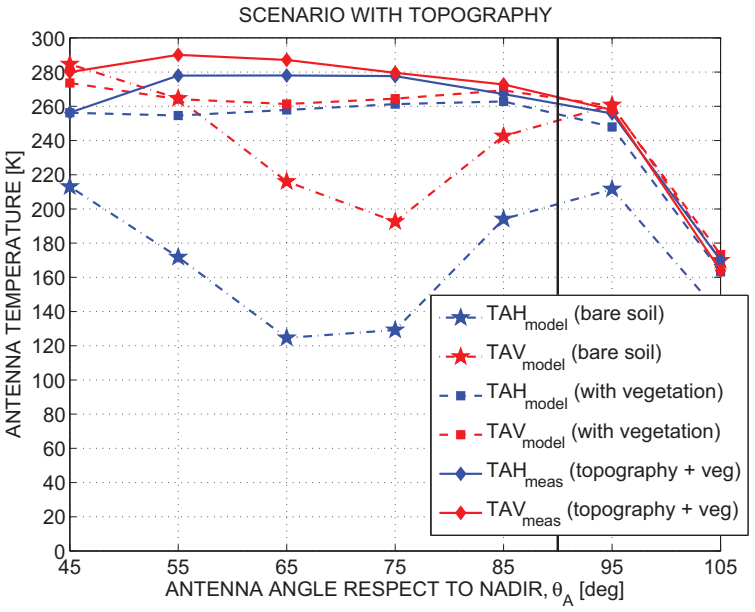

(b)

Fig. 8.3: Measurements (solid lines) and simulated (dashed lines) antenna temperatures at H and V polarisations as a function of the antenna observation angle referred to nadir. Simulations correspond to (a) an hypothetical scenario without topography, with and without vegetation; and, (b) mountainous scenarios, with and without vegetation. The solid vertical line depicted at $\theta_A = 90°$ indicates that the radiometer boresight is horizontal.

to the horizon.

In Fig. 8.3(a), simulations have been performed with an hypothetical flat surface scenario. As it can be observed, simulations' trend differs from measurements if topography is not taken into account. Simulated antenna temperature rapidly decreases for $\theta_A > 65°$, because of the large local incidence angle and the presence of the sky within the radiometer beam. On the contrary, the decrease in the measured antenna temperature is only significant above $\theta_A > 95°$, when the sky almost fills the antenna beam. On the other hand, Fig. 8.3(b) shows simulations of the mountainous scenario, that is, the DEM of the site has been used. In this case, if the vegetation effect is not simulated using (3.26), results differ from measurements although at large observation angles the agreement is already much better than in Fig. 8.3(a). If the vegetation canopy is simulated, the agreement is quite good over the whole range of antenna incidence angles. In this case, the largest discrepancies between measurements and simulations, up to 20 K, are observed only at low antenna elevation angles ($\theta_A < 65°$), which correspond to the largest local incidence angles.

Finally, Fig. 8.4 shows the measured and simulated antenna temperature images as a function of the observation direction referred to the antenna reference frame. The sixth day of experiment has been chosen as representative since the atmospheric, soil, and vegetation conditions were almost identical during the experiment. Simulations agree with measurements except for a nearly bare area near the radiometer, where the local incidence angle is high ($\theta_{\text{local}} > 65°$). Differences are larger at H than at V-polarisation, which suggests that improvements in the model are still needed for this case.

8.5 Conclusions

The TuRTLE 2006 ground based field experiment was conducted at El Brull, Parc Natural del Montseny, 50 km north of Barcelona, Spain, in May 2006. The valley in front of the radiometer was observed at seven incidence and nine azimuth angles, covering the entire mountain slope and the mountain-to-sky transition. The antenna brightness temperature was derived from measurements, and then compared to numerical simulations.

The agreement between simulations and radiometric measurements, show the large impact on the land emission of the vegetation cover and topography through the variations in the local incidence angle due to topography. This demonstrates that vegetation and topography effects can be accounted for by using a land cover map, a high resolution DEM, and a facet model to properly compute the variations of the local incidence angle, the polarisation mixing, and the antenna pattern averaging.

At the SMOS scale, this work confirms the applicability of facet models when dealing with topography as was done in Talone *et al.* [2007]. The largest discrepancies occur for almost bare soils at large local incidence angle and H-polarisation, which suggests that further modeling work is still needed in this case.

Airbone experiments over high topography areas would be necessary to increase the existing data set, and to provide observations of larger pixels as is the case of SMOS. Ground

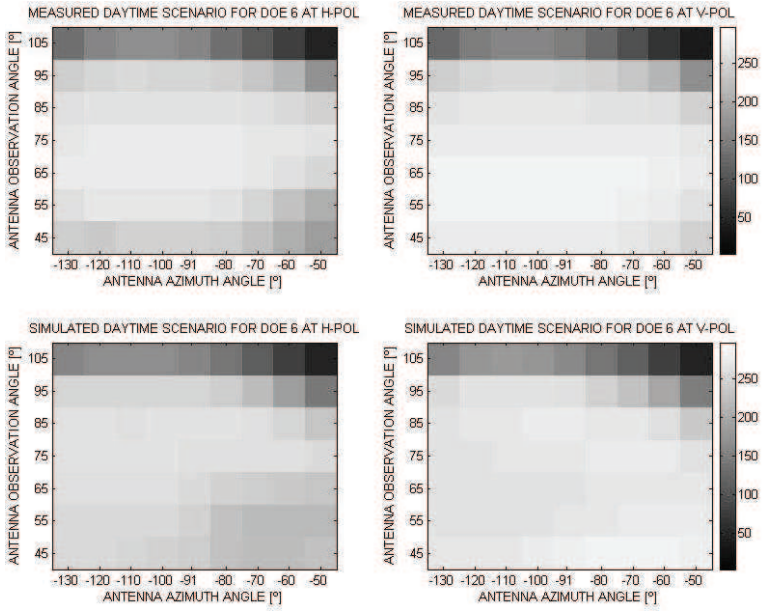

Fig. 8.4: Measured (above) and simulated (below) antenna brightness temperature at H and V polarisations on the sixth day of experiment. Results are representative of the whole experiment since the atmospheric, soil, and vegetation conditions were almost identical during the whole field campaign.

data should be taken homogeneously and intensively at high density concurrently with airborne measurements.

Chapter 9

Other variables affecting the land emission

Previous chapters have focused on the impact of soil roughness and texture, vegetation (vines), and topography on the radiometric measurements at L-band. These parameters have been identified as important factors affecting the L-band emission that must be well characterised to estimate the soil moisture content from microwave radiometers measurements. In this chapter, a brief summary of the state of the art of other factors which may impact the land emission is presented for completeness of this Ph.D. Thesis.

9.1 Reflection of Sun emission over land surfaces

Sun brightness temperature at L-band ranges from 10^5 K to a million Kelvin depending on the solar activity. This strong emission can affect the radiometric measurements in two ways: (i) directly, intercepted by the main or side lobes of the antenna radiation pattern, and (ii) indirectly, through reflection on the Earth's surface (known as Sun glint). Sun effects in 2-D aperture synthesis radiometry imaging, cancellation techniques to remove them [Camps *et al.*, 2004], and Sun glint impact on the sea surface salinity retrieval [Reul *et al.*, 2007, Vine *et al.*, 2005, Camps *et al.*, 2005b] have been already studied in the context of the SMOS mission. However, few studies have been performed to assess the land emission increase due to Sun and its impact on the soil moisture retrieval, since soil reflectivity is smaller than water reflectivity and, thus, Sun glint contribution over land is expected to be lower than over sea. Escorihuela *et al.* [2008] uses ground based and airbone data from the SMOSREX and NAFE06 experiments, respectively, and points out an average increase in brightness temperature at H(V)-pol of 17(7) K over an agricultural area and for a zenith angular difference of 14° and an azimuth angular difference of 20° between the radiometer (bandwidth of 14° across track and 17° along track) and the Sun during NAFE06. An increment of 25 K at H-pol and 17 K at V-pol are found out over grass in the SMOSREX site for a radiometer with a 13.6° beamwidth and an incidence angle of 40° .

As a small contribution to this issue, direct and reflected Sun measurements were acquired at some moments during the T-REX 2006 experiment at Agramunt, Spain. Some results are given hereafter.

9.1.1 Solar radio flux

The solar radio flux F_λ is defined as the brightness at wavelength λ integrated over the solar disc. Since the solar disc is small, F_λ in $\mathrm{W{\cdot}m^{-2}{\cdot}Hz^{-1}}$ can be approximated to

$$F_\lambda = B_{\mathrm{sun}}\Omega_{\mathrm{sun}} \tag{9.1}$$

where Ω_{sun} is the solid angle of the Sun as viewed from the Earth, $\Omega_{\mathrm{sun}} = 8.22 \cdot 10^{-5}$ sr, and B_{sun} is the mean brightness expressed in $\mathrm{W{\cdot}m^{-2}{\cdot}Hz^{-1}sr^{-1}}$. Several stations around the world are continuously measuring the solar flux at various wavelengths. Daily solar flux data at 1.415 GHz expressed in solar flux units (sfu; 1 sfu = 10^{-22} $\mathrm{W{\cdot}m^{-2}{\cdot}Hz^{-1}}$) are available from the four observatories in the Radio Solar Telescope Network (RSTN): Sagamore Hill and Palehua (USA), San Vito (Italy), and Learmonth (Australia). These data can be accessed online through the National Geophysical Data Center at Boulder RST [n.d.].

9.1.2 Sun brightness temperature

Assuming that the Sun is a uniform black-body and using the Rayleigh-Jean approximation, the integrated solar brightness temperature $T_{\mathrm{sun}}(t)$ expressed in Kelvin can be estimated from the solar flux $F_\lambda(t)$ as

$$T_{\mathrm{sun}}(t) = \frac{\lambda^2}{2k\Omega_{\mathrm{sun}}} F_\lambda(t) 10^{-22} \tag{9.2}$$

where k is the Boltzmann's constant. At L-band, this expression can be approximated to

$$T_{\mathrm{sun}} \approx 2000 F_{\text{L-band}} \tag{9.3}$$

where $F_{\text{L-band}}$ is the solar flux at 1.415 GHz in sfu.

9.1.3 Sun antenna brightness temperature

The direct contribution from the solar radiation to the radiometer antenna temperature can be obtained from the normalised antenna radiation pattern F_n and the beam solid angle Ω_p as

$$T_A = \frac{1}{\Omega_p} \int T_{\mathrm{sun}}(\Omega) F_n(\Omega) d\Omega. \tag{9.4}$$

If the integration range is small and the solar brightness temperature is constant, then (9.4) can be approximated to

$$T_A = \frac{T_{\mathrm{sun}} F_n \Omega_{\mathrm{sun}}}{\Omega_p}. \tag{9.5}$$

Substituting T_{sun} for the expression in (9.2) and knowing that the antenna gain is $G = (4\pi/\Omega_p)F_n$, then

$$T_A = 0.013 F_{\text{L-band}} G. \tag{9.6}$$

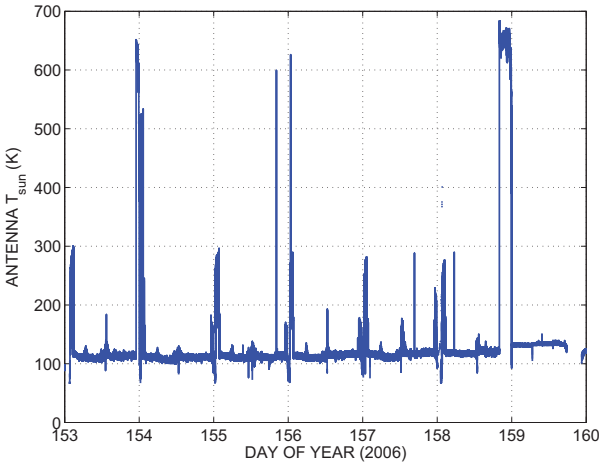

Fig. 9.1: Antenna brightness temperature of Sun at 1.4 GHz computed from solar flux measurements conducted at San Vito RSTN station (Italy) RST [n.d.], and LAURA antenna gain.

In the same manner, the value of the reflected Sun contribution can be estimated by multiplying the land reflection coefficient by the sun antenna brightness temperature computed from (9.6) using the appropriate directional gain. Detailed computations would involve the integration of the bistatic scattering coefficients Ulaby & Dobson [1989], but this is out of the scope of this work.

Values of T_A at 1.4135 GHz during the first week of June, 2006, using as inputs to (9.6) the solar flux measurements conducted at the San Vito station, and the LAURA radiometer gain at the main lobe (20 dB) are represented in Fig. 9.1.

9.1.4 Radiometric observations of Sun

The radiometric data was acquired during the first week of June, 2006, in Agramunt, Spain (41° 81N, 1° 1W, 356 m altitude). The experiment site consisted of a bare field, with a constant soil moisture of 4% and a standard deviation of the height profile of 1 cm, see Fig. 9.2.

The LAURA radiometer was located at a bare field looking westwards. Measurements were

Fig. 9.2: The LAURA radiometer at the T-REX 2006 experiment site during the Sun measurements.

continuously acquired from 4 p.m. until sunset, which corresponded to solar elevation angles from 60° to 0° with respect to the line of horizon. LAURA was oriented so that the main lobe pointed above the Sun position, and then automatic measurements at descending radiometer elevation angles were acquired until an elevation angle of 55° with respect to nadir. This strategy was repeated until sunset, and allowed the acquisition of the direct and reflected contributions to the measured brightness temperature coming from the solar radiation. Measurements were calibrated using a microwave absorber and the sky as hot and cold load targets, respectively. The down-welling atmospheric brightness temperature was computed from numerical models that include the antenna orientation and pattern, its geographical coordinates, the galactic noise map at 1420 MHz [Reich & Reich, 1986], the date and time of measurements, and weather parameters.

Sample brightness temperatures at V- and H-pol corresponding to June 8, 2006, are represented in Fig. 9.3. LAURA measurements at antenna angles from 80° to 115° from zenith at H- (blue solid line) and V-pol (red solid line) are compared to simulations (icons) carried out using the Wang & Choudhury [1981] model for the soil brightness temperature and numerical methods for the sky brightness temperature. Green lines in Fig. 9.3 indicate the difference between simulations and measurements.

An increment of 130 K on the brightness temperature at both polarisations is observed when LAURA's main antenna beam pointed the Sun. This is in accordance with theoretical estimates using (9.6) and Fig. 9.1 (floor value between peaks), and indicates that solar radiation seems to be polarisation independent (at least in these measurements). However, no significant increment on the land brightness temperature due to Sun glint has been detected in measurements at the range of incidence angles from 90° to 60° respect to nadir, which seems to indicate that scattered Sun may not be a problem in SMOS, where scattering angles are larger than 45° , and typically around 65° . This suggests that Sun glint over land is negligible due to the low value of the terrain scattering coefficients (lower than -20 dB) at incidence angles larger than 45° [Ulaby & Dobson, 1989].

Since the Sun scattered radiation over land is much smaller than that over sea, and we recall that the scattering takes place in the alias region that is not imaged by the instrument [Camps *et al.*, 2005a], we can conclude that the spill over of the scattered Sun will be even smaller and, to all effects, most probably negligible in the SMOS case.

9.2 Dew

The observed effect of dew on brightness temperature at L-band is rather low in comparison to much more sensitive elements such as soil moisture, soil roughness, or vegetation water content. Some initial studies concluded that signal was almost insensitive to dew Jackson & Moy [1999], Wigneron *et al.* [1996]. Recent studies, however, point out some variations in the radiometric measurements due to dew but with different conclusions. For instance, Hornbuckle & England [2004], Hornbuckle *et al.* [2006, 2007] analyses the effects of dew on a corn field and reports a 2 to 4 K decrease in the brightness temperature, specially at V-pol. On the contrary,

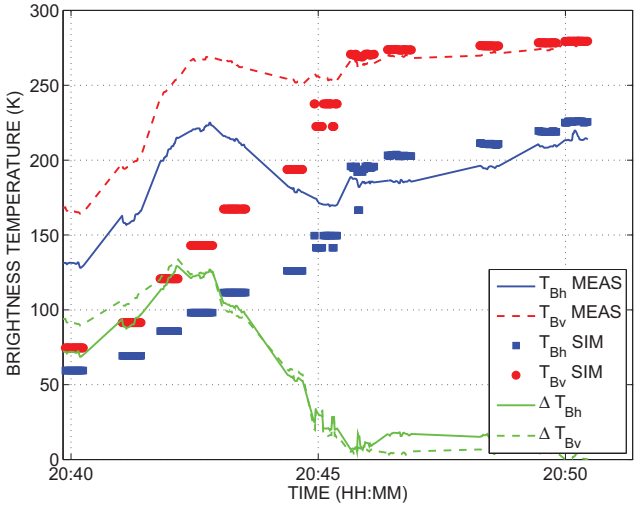

Fig. 9.3: Brightness temperature at V- and H-polarisations corresponding to June 8, 2006, at antenna elevation angles from 100° to 65° from nadir. Measurements from LAURA (solid blue and red lines), simulations (icons), and the difference between both of them (green lines) are represented.

de Jeu *et al.* [2004] notes an increase of 5 K over a grass field. Escorihuela *et al.* [2009] observes an increase of 0.5 and 1 K over a grass field at V- and H-pol, respectively, some time after dew and suggests that it is due to the absorption of dew water by litter, so that the diurnal variations of vegetation water content should be taken into account when studying the effects of dew.

9.3 Rain interception by the vegetation canopy and understorey

The matter of rain interception has also been studied by some authors in the attempt to model land emission when there exists a vegetation canopy above the soil. In addition to the standing vegetation, there may exist a layer understorey which may be considered transparent to the microwave emission if dry [Jackson & Schmugge, 1991], but which becomes an important microwave absorber and emitter when wet [Schmugge *et al.*, 1988, Saleh *et al.*, 2007b]. This leads to a lower sensitivity of brightness temperature to soil moisture.

Putuhena & Cordery [1996] estimated the maximum interception by several types of forest understorey as a function of the dry biomass, thickness, and fraction cover. They concluded that the water intercepted by understorey represented between once and twice the dry vegetation biomass for leaf type litters, and a lower percentage for stem and branch litters. Wigneron *et al.* [1996] reported that intercepted water increased the emission at C-band and H-pol and proposed a bi-frequency technique to estimate soil moisture and soil water content and storage during irrigation. Finally, Saleh *et al.* [2006a,b] noted the possibility of flagging the presence/absence of rain interception by the standing vegetation based on the polarisation ratio at 50° . However, Saleh et al. could not develop an interception flag for the understorey.

9.4 Frozen soils and snow

Frozen soils cover large areas at high latitudes and can be expected in winter in many areas of the Earth. Since the dielectric properties of frozen soil are close to those of dry soil Mätzler [1994], soil moisture retrieval algorithms may offer a misleading result. Zhang *et al.* [2003] extended the semi-empirical dielectric mixing model for soil water mixture to describe the dielectric constant change of frozen soil as a function of temperature. The authors reported that freezing has a strong effect on the dielectric constant of soil, particularly at the beginning of freezing. Schwank *et al.* [2004] found out good agreement between measurements of freezing soils and impedance-matching models of the air to soil transition layer.

On the other hand, snow has very different dielectric properties. Fresh, dry snow is transparent to microwave radiation, but as snow melts its dielectric constant increases and may be totally opaque to microwave radiation when wet. At present, the L2SM prototype processor includes a flag for snow covered areas and the soil moisture retrieval will not be attempted in these situations [Kerr *et al.*, 2006]. Macelloni *et al.* [2006, 2007] shows some results of the DOMEX 2004 experiment, aimed to test the stability of L-band emission of the Antarctic plateau. The authors confirm the high spatial and temporal stability of the snow layers and the possibility of using the Dome-C plateau as a calibration target for future spaceborne radiometer missions such as SMOS.

9.5 Conclusions

Although it is known that solar radiation at L-band can be an important source of interference, few studies have been performed to assess the land emission increase due to Sun. Direct and reflected Sun measurements were acquired in June 2006 in Agramunt, Lleida (North-East of Spain). The LAURA radiometer was oriented so that the main lobe pointed above the Sun position, and then automatic measurements at descending radiometer elevation angles were acquired until an elevation angle of 55° with respect to nadir. This strategy was repeated until the Sun set, and allowed the study of the direct and reflected contributions to the measured brightness temperature coming from the solar radiation.

The sky brightness temperature at both polarisations increases 130 K when the Sun enters the radiometer's antenna main beam. This is in accordance with theoretical estimates, and indicates that solar radiation is polarisation independent. No significative increment on the soil brightness temperature due to Sun glint has been detected in the data. This suggests that Sun glint over land at high incidence angles is negligible due to the low terrain scattering coefficients at these incidence angles.

Dew, rain interception, snow, freezing soils have been not studied in this Ph.D. Thesis but, as has been pointed out in the outline given in this Chapter, are among the factors influencing the emission of land surfaces.

Chapter 10

Conclusions and future lines

The present Ph.D. Thesis has been performed in the context of the Soil Moisture and Ocean Salinity (SMOS) mission pre-launch activities over land. A summary of the state-of-the-art of ground- and space-borne sensors, and of experiments involving radiometric sensors and dealing with soil water content measurements is given in Chapter 1. Then, the basic concepts of microwave radiometry and of soils physics and land emission modelling are presented in Chapters 2 and 3, respectively. A description of the field campaigns over land carried out by the UPC during the last years is provided in Chapter 4. The execution of these experiments, the data processing, and the physical interpretation of measurements constitutes the core of this Ph D Thesis. Emissivity of land surfaces depends upon the interaction of several soil and vegetation characteristics such as soil moisture, roughness, and temperature, and vegetation opacity and albedo. Data analysed in this work was acquired in experiments performed over vineyards (SMOS REFLEX 2003/2006), different types of flat bare smooth soil (MOUSE 2004), fields with different plough, but the same soil type (T-REX 2004/2006), and mountainous sites (TuRTLE 2006). Measurements were acquired using the L-band Automatic Radiometer (LAURA) which has a working frequency of 1.4 GHz, the same as SMOS payload, MIRAS. Results from the experimental campaigns are given in Chapters 5 to 9. Main conclusions are outlined in the following sections.

10.1 Conclusions on soil texture, soil roughness, vines, and topography effects

Soil texture influences the electromagnetic behaviour of soils since it affects their dielectric constant. During MOUSE 2004, six types of bare flat soils with different soil moisture contents were measured at five incidence angles. As expected, variations on the moisture profile were noted depending on texture.

The emission of loams and sands showed a linear dependence on the percentage of field capacity, especially at H-pol. In this case, the R-squared estimator at θ=35° was found to be between 70% and 85%. On the contrary, clay showed no linear trend which, however, can not

be a general conclusion since clay data had a large scattering.

Soil emissivity was derived from radiometric measurements, and then soil moisture was retrieved using three different expressions for the soil dielectric constant: the semi-empirical models by Wang & Schmugge [1980] and Dobson *et al.* [1985], and polynomials derived from laboratory measurements of MOUSE 2004 soil samples. The modified Wang & Choudhury [1981] soil emission model, with Q_s=0 and n=0, was used as forward model in the retrieval algorithm. Best results were obtained when no constraints were applied to soil moisture and temperature. The estimated soil moisture was compared with the soil moisture measured at different depths. For loam and ferromagnetic soils best results were achieved considering as ground-truth data the soil moisture in the 0–5 cm layer, 0–15 cm layer for sands, and 0–10 cm layer for clays. On the other hand, when results for every dielectric constant model were compared, it was found out that the Wang & Schmugge [1980] model had a better performance in the retrieval algorithm of loam and ferromagnetic soils, while the Dobson *et al.* [1985] model offered best results for sands.

Results from MOUSE 2004 suggest that: (i) the SMOS Level 2 soil moisture processor should select the soil dielectric constant model as a function of texture, since the root mean squared error can vary from 2% to 7% depending on the soil texture, and (ii) soil moisture estimates will be the averaged value in a soil layer which will depend on texture.

Soil roughness has a strong impact on land brightness temperature. This effect is more noticeable in the case of dry soils. Data from bare soils with a standard deviation of height varying from 8 mm to 33 mm was acquired during the T-REX experiments, and was compared to predictions from numerical and semi-empirical soil emission models. The goodness of these models is of key importance for an accurate soil moisture estimation from SMOS data.

As expected, dry soil emissivity at H-pol decreased almost linearly with increasing incidence angle, being the decrement inversely proportional to soil roughness. Although similar emission was measured at H-pol for all plough at low incidence angles, it was noted that emission decreases slowly for rough soils than for smooth soils. Above $\theta = 50^\circ$, the decreasing slope of H-pol emission was higher for all plough.

The sensitivity of V-pol to roughness is lower than that of H-pol. The trend of V-pol emission was found to be different depending on whether the soil was wet or dry. When the soil is wet the emission increased with the incidence angle, which is in accordance with most model predictions. However, the trend for dry soils is decreasing with increasing incidence angle and roughness. This may suggest the existence of a relationship between soil moisture and the effective roughness.

The integral equation method (IEM) predicts an increase in V-pol emission with incidence angle, which is not in accordance with measurements of dry soils. On the other hand, the descending predicted descending trend at H-pol with increasing incidence angle is in accordance to measurements, although IEM underestimates the soil emission both for dry and wet soils. In a randomly ploughed field, without a significant tillage direction, the impact of choosing an exponential or gaussian height probability density function in the IEM model is minimum, whereas it was noted that the incoherent term of the reflectivity must be considered for rough soils.

In general, all semi-empirical land emission models follow the trend of dry soils measurements at H-pol, whereas discrepancies exist for wet soils. Neither the semi-empirical models nor the IEM describe the trend of dry soils V-pol measurements, being the error at this polarisation larger as the incidence angle increases. The lowest error between predictions and measurements for H-pol was obtained using the Wang & Choudhury [1981] model, but with the λ-windowing standard deviation of height instead of the standard deviation calculated from the height profile. The dependence on the incidence angle proposed by Wang & Choudhury (a squared cosine) had been discussed by other authors which considered it to be too much strong at L-band. However, this simple formulation has been tested with T-REX data with good results if the "averaged" standard deviation in λ transects is used.

The SMOS REFLEX 2003/2006 experiments site was in the Valencia Anchor Station, a selected area for the SMOS calibration and validation activities. No previous studies over vines were reported in the literature prior to these campaigns. In the first experiment, fully developed vines were characterised during two weeks, while controlled irrigations moistened the field. The second experiment was planned to monitor changes in the L-band emission of vineyards during different stages of plants development.

Since vines do not have a predominant vertical nor horizontal structure, the opacity and the albedo were found to be independent on the polarisation. The Wang & Choudhury [1981] model was used as the soil emission forward model in the retrieval algorithm, while the dielectric constant model was the one from Wang & Schmugge [1980]. Good results were obtained for incidence angles up to 55° , but he the convergence of the algorithm was rarely achieved above that value. The error between ground-truth and estimated soil moisture was 2.3%, better than the 4% required for SMOS. For incidence angles above 55° the convergence of the algorithm was rarely achieved, probably due to the larger effect of the vegetation at large incidence angles, not accurately described by the model. Higher order models should be accounted for at these angles.

A diurnal oscillation of the emissivity, with a maximum around noon (if no rain) and a peak-to-peak variation in the emissivity up to 0.05, was noted during SMOS REFLEX 2006, most probably due to changes in the plants diurnal water balance. This highlights the importance of having concurrent SMOS and ground-truth data during the CalVal activities. H-pol emissivity is more sensitive to changes in plants and soil moisture than V-pol. However, in the presence of rocks above the soil, the sensitivity of H-pol emissivity to soil moisture decreases since (i) the increase in the rock fraction increases the effective soil roughness, and (ii) the dielectric constant of rocks is lower than that of wet soils. The trend of the emission as a function of ground-truth soil moisture was almost constant at the rocks side, since the radiometer did not sense changes on the soil emission because of rocks. This will lead to an underestimation of the soil moisture content by the retrieval algorithms.

Although the radiometric behaviour varies from one canopy to the other, at a larger scale such as that of SMOS it is very likely that the vegetation types can be averaged over the footprint and that it is not necessary to account for an accurate distinction between canopies.

Soil moisture retrieval from SMOS data will not be attempted for pixels which have been

previously flagged because of their high topography. However, soil moisture will be retrieved at mid- and low-topography pixels so an understanding of the effects of topography on the radiometric signal is necessary. Radiometric measurements over a valley were acquired during TuRTLE 2006 at seven incidence and nine azimuth angles, covering the entire mountain slope and the mountain-to-sky transition. The antenna brightness temperature was derived from measurements, and then compared to numerical simulations.

The agreement between simulations and radiometric measurements, show the large impact on the land emission of the vegetation cover and topography through the variations in the local incidence angle due to topography. Vegetation and topography effects can be accounted for by using a land cover map, a high resolution digital elevation map, and a facet model to predict variations of the local incidence angle, the polarisation mixing, and the antenna pattern averaging. Topography effects can not be neglected and accounted for only by the introduction of the vegetation canopy. The largest discrepancies were noted for almost bare soils at large local incidence angle and H-polarisation, which suggests that further modelling work is still needed in this case. At the SMOS scale, results confirm the applicability of facet model in mountainous scenarios, as was tested with simulations in Talone *et al.* [2007].

10.2 Future lines and recommendations

The development of improved soil emission models should be a priority in view of the upcoming missions devoted to the measurement of soil moisture from space. These must include a better parametrisation of the soil texture variability, the soil surface roughness, and of the transition layer between atmosphere and soil.

Scientific requirements demand an error in soil moisture estimates from SMOS data lower than 4% so that soil moisture maps can be assimilated by hydrology models. This value is the same as the tolerance of widely used hand-held soil moisture probes which measurements are assumed as ground-truth data. Moreover, on the contrary to the sea surface salinity case where spatio-temporal averaging is foreseen to improve the salinity estimates, in the case of soil moisture its high spatial and temporal inhomogeneity complicates even more the correlation between predictions and reality. The to-do list after SMOS launch is large, but important goals can be achieved at the end of the process.

Few months before SMOS launch, there are still many open issues regarding the soil moisture retrieval far from being closed. The experimental research performed in the past years has improved our understanding of soil physics and has contributed to tune the existing land emission models. However, this tuning has been achieved most of the times at the plot scale, with coefficients obtained by best-fit for each particular scenario. We will have to wait for SMOS measurements to see whether these results can be applied to a general case and to a pixel with a size of the order of 50 km $\times$ 50 km. The selection of one forward model or the other shall also have to wait for SMOS data to be available.

Other airborne field experiments would be necessary to increase the existing data set, and to provide observations of larger pixels. These data could also be used to test pixel desaggrega-

tion techniques with which to improve the resolution of SMOS, particularly important for soil moisture applications.

Another interesting research line would be the combined use of radiometry and GNSS-R reflectometry for soil moisture estimates. Soil moisture retrieval has already been satisfactorily achieved by means of GNSS-R reflectometry [Rodríguez-Alvarez *et al.*, 2008]. With this scope is being performed the long-term GPS and RAdiometric Joint Observations experiment (GRAJO) in Vadillo de la Guareña (Zamora), in the REMEDHUS site, which will be used also for SMOS calibration and validation activities. At the plot-scale, the goal is to jointly use radiometry and GPS-reflectometry data to study: (i) the influence of the vegetation on the retrieval of geophysical parameters, and (ii) to characterise the roughness factor. Apart from this, a land brightness temperature simulator of the site will be implemented together with disaggregation and soil moisture retrieval algorithms to estimate soil moisture from airbone radiometric measurements. This line of investigation may continue in parallel to SMOS calibration/validation field experiments to improve the final soil moisture product and the performance of an hypothetical SMOSops mission.

Appendix A

Numerical simulations of vegetation canopies

In this appendix the fundamental of the EMISVEG tool are presented. EMISVEG is a numerical model developed at the UPC to efficiently compute the complete modified Stokes emission vector (see Section 2.2.5) of vegetation-covered soils at low microwave frequencies over a wide range of incidence angles. This tool was implemented by Martínez-Vázquez et al. [Martínez-Vázquez *et al.*, 2002, Ledesma, 2003] and its description has been included here only for completeness. EMISVEG was used to simulate the SMOS REFLEX 2003 site. Results have been briefly described in Section 7.3.7 and have been submitted for publication [Martínez-Vázquez *et al.*, 2009].

A.1 The polarimetric radiative transfer equation

The polarimetric emission, which is one of the key observables in radiometry, can be computed by means of the radiative transfer equation (RTE) [Tsang *et al.*, 2000, pp. 281-282]:

$$\frac{d\bar{e}(\theta,\varphi)}{ds} = -\bar{\bar{k}}_e(\theta,\varphi)\bar{e}(\theta,\varphi) + \bar{F}(\theta,\varphi) + \int_0^{2\pi}\int_0^{\pi} \bar{\bar{P}}(\theta,\varphi,\theta',\varphi')\bar{e}(\theta,\varphi)d\Omega' \tag{A.1}$$

where the extinction matrix $\bar{\bar{k}}_e$ is given by p.274]:

$$\bar{\bar{k}}_e = \frac{2\pi n_0}{k}\begin{bmatrix} 2\Im(f_{vv}) & 0 & \Im(f_{vh}) & -\Re(f_{vh}) \\ 0 & 2\Im(f_{hh}) & \Im(f_{hv}) & \Re(f_{hv}) \\ 2\Im(f_{hv}) & 2\Im(f_{vh}) & \Im(f_{vv}+f_{hh}) & \Re(f_{vv}-f_{hh}) \\ 2\Re(f_{hv}) & -2\Re(f_{vh}) & \Re(f_{hh}-f_{vv}) & \Im(f_{vv}+f_{hh}) \end{bmatrix}, \tag{A.2}$$

being n_0 the number of particles per unit of volume, k the wave number, and f_{pq} the forward scattering amplitudes, which are computed as the sum of the forward scattering amplitudes of each individual scatterer (branches, leaves, ...).

The emission vector $\bar{F}$ in (A.1) is given by [Tsang *et al.*, 2000, p. 282]:

$$\bar{F}(\theta,\varphi) = \left[\begin{array}{cccc} k_{a1}(\pi-\theta,\pi+\varphi) & k_{a2}(\pi-\theta,\pi+\varphi) & -k_{a3}(\pi-\theta,\pi+\varphi) & -k_{a4}(\pi-\theta,\pi+\varphi) \end{array} \right]^T, \tag{A.3}$$

where

$$k_{a1}(\theta,\varphi) = k_{e11}(\theta,\varphi) - \int \left[P_{11}(\theta,\varphi,\theta',\varphi') + P_{21}(\theta,\varphi,\theta',\varphi')\right] d\Omega', \tag{A.4}$$

$$k_{a2}(\theta,\varphi) = k_{e22}(\theta,\varphi) - \int \left[P_{12}(\theta,\varphi,\theta',\varphi') + P_{22}(\theta,\varphi,\theta',\varphi')\right] d\Omega', \tag{A.5}$$

$$k_{a3}(\theta,\varphi) = 2k_{e13}(\theta,\varphi) + 2k_{e23}(\theta,\varphi) - 2\int \left[P_{13}(\theta,\varphi,\theta',\varphi') + P_{23}(\theta,\varphi,\theta',\varphi')\right] d\Omega', \tag{A.6}$$

$$k_{a4}(\theta,\varphi) = -2k_{e14}(\theta,\varphi) - 2k_{e24}(\theta,\varphi) + 2\int \left[P_{14}(\theta,\varphi,\theta',\varphi') + P_{24}(\theta,\varphi,\theta',\varphi')\right] d\Omega', \tag{A.7}$$

$$\tag{A.8}$$

The phase matrix $\bar{\bar{P}}(\theta,\varphi,\theta',\varphi')$ is given by [Tsang *et al.*, 2000, pp.126 and 271]:

$$\bar{\bar{P}}(\theta,\varphi,\theta',\varphi') = n_0 \left[\begin{array}{cccc} |f_{vv}|^2 & |f_{vh}|^2 & \Re(f_{vh}^* f_{vv}) & -\Im(f_{vh}^* f_{vv}) \\ |f_{hv}|^2 & |f_{hh}|^2 & \Re(f_{hh}^* f_{hv}) & -\Im(f_{hh}^* f_{hv}) \\ 2\Re(f_{vv} f_{hv}^*) & 2\Re(f_{vh} f_{hh}^*) & \Re(f_{vv} f_{hh}^* + f_{vh} f_{hv}^*) & -\Im(f_{vv} f_{hh}^* - f_{vh} f_{hv}^*) \\ 2\Im(f_{vv} f_{hv}^*) & 2\Im(f_{vh} f_{hh}^*) & \Im(f_{vv} f_{hh}^* + f_{vh} f_{hv}^*) & \Re(f_{vv} f_{hh}^* - f_{vh} f_{hv}^*) \end{array} \right]. \tag{A.9}$$

In (A.2) and (A.99) the f_{pq} coefficients are the vector-scattering amplitude functions that provide the amplitude, phase and polarisation information of the scattered field at q-polarisation $\vec{E_q} = \hat{e_q} f_{pq}(\theta,\varphi,\theta',\varphi') e^{-jkr}/r$, when a plane wave at p-polarisation $\vec{E_i} = \hat{e_p} e^{-j\vec{k}_{\rm inc}\vec{r}}$ is incident on each scatterer.This expression assumes a far-field situation, so the interaction between near particles, such as leaves and grapes in a vine, is neglected.

The solution of (A.1) entails the following boundary conditions:

- $T_{{\rm up},p}(\theta,\bar{\varphi},z=0)$ is the soil's surface emission, and
- $T_{{\rm dn},p}(\theta,\bar{\varphi},z=h)$ is the down-welling atmospheric emission at the top of the vegetation layer.

Since the soil emission ($T_{{\rm up},v}$ and $T_{{\rm up},h}$) and the vegetation emission at L-band are larger (about two orders of magnitude) than the atmospheric down-welling contributions, as a first approximation $T_{{\rm dn},p}(\theta,\bar{\varphi},z=h)$ could be neglected at nadir. Nevertheless, since different elevation angles are considered in the analysis performed in section 5, both the atmospheric downwelling contribution (2.1 K at nadir) and the cosmic background (2.7 K at nadir) are accounted for in EMISVEG, corrected by the cosine of the elevation angle, which is a good approximation up to the maximum incidence angles we are dealing with.

In the computation of the phase matrix in (A.9) the interaction between the vegetation elements and the soil has been considered up to first order. This includes: (i) the direct scattered field, (ii) the scattered field when the incident field is reflected on the soil, (iii) the scattered field reflected on the soil when the incident field impinges directly to the element, and (iv) the combination of b) and c). This assumption together with the far-field simplification helps to maintain the overall computation complexity at an affordable level.

A.2 Geometric description of the SMOS REFLEX 2003 site

A uniform distribution of plants was used for modelling man-made scenarios such as the SMOS REFLEX 2003 vineyard. To simplify the computation of the radiometric results, the vine model was repeated within the illuminated area. The geometric description of the different components used to model the scenario, with particular emphasis on the elements used to model the vines, is presented in the following sections.

A.2.1 Soil surface

The soil at the site was modelled as a Gaussian rough surface characterised by its rms height (σ_h) and their correlation lengths $l_x = l_y = l$. Actually a plowed terrain may present different correlation lengths in the X and Y directions, thus inducing an azimuthal effect on the Stokes elements. No slope of the terrain was considered.

A.2.2 Trunks and branches

The vegetation layer was modelled by a set of simple discrete scatterers for which an analytical formulation for the scattered fields exists. Trunks and branches are dielectric cylinders, optionally with an external corrugation, which are arranged following a fractal geometry described by Lindenmayer systems (L-systems) [Prusinkiewicz & Lindenmayer, 1990]. An iterative method and rules describing the growth from the tree trunk to the branches, is schematically shown in Fig. A.1. Figure A.2 shows a detail of the leaves in a terminal branch, a sample of cereals and rice, and examples of the final stage of other types of plants generated with a fractal geometry. Each element in the plant is characterised by its centre position in the tree reference frame ($\vec{r}_j$), its orientation ($\vec{k}_j$), its length (L_j), and radius (R_j). Similarly, each plant is characterised by its point of birth over the field of view ($\vec{r}_{k,\mathrm{trunk}}$), having for each scatterer the absolute position in the global frame of the illuminated area.

The model used for vines is shown in Fig. A.3. It includes leaves, and an external corrugation to model the roughness of the trunk and branches.

A.2.3 Stems and leaves

Stems and leaves were added to the tree model using an algorithm based on the density of these elements so as to adjust the leaf area index (LAI) [Martínez-Vázquez *et al.*, 2002]. Stems, like branches, were modelled by dielectric cylinders, optionally with an external corrugation.

Fig. A.1: Random tree distribution over a rough soil inside the illuminated area (leaves not drawn)

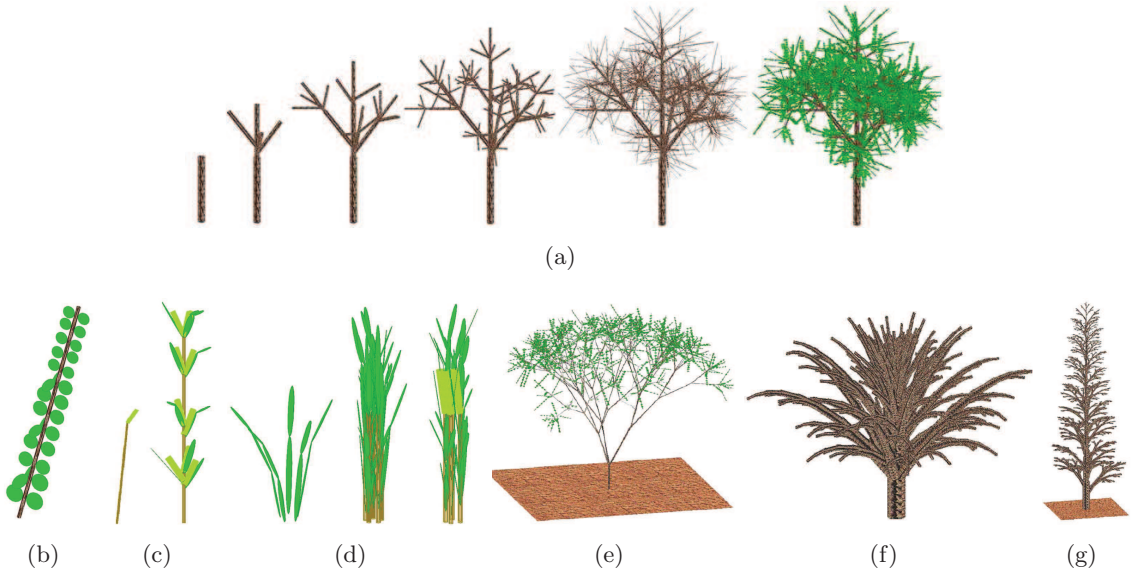

Fig. A.2: (a) Iterative growing process of a tree, (b) Detail of leaves in a terminal branch, (c) Samples of cereals, (d) Clusters of agricultural crops, (e) Sample of bush, (f) Sample palm tree, and (g) Sample of deciduous tree.

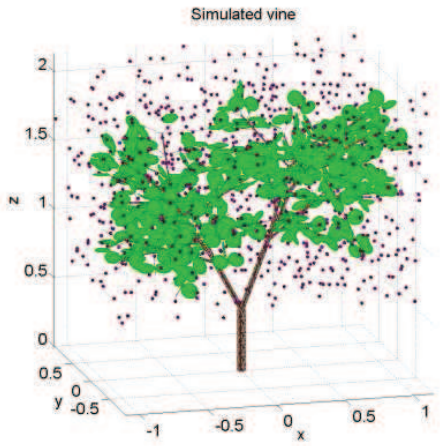

Fig. A.3: Geometric model of a vine with fruits

Leaves were modelled as flattened ellipsoids in one dimension (disc: flat leave) or in two dimensions (needles), and were positioned only over the stems. Due to the large number of leaves per plant, the set of possible sizes and orientations was discretised so that the total computation time remained acceptable. For the vine model in Fig. A.3, each final branch has between 6 and 12 stems (uniformly random distributed), and each stem holds a number of leaves that covers all the stem length. Leaves are modelled as disks (flattened ellipsoids in one dimension).

A.2.4 Fruits

Grapes were modelled as dielectric spheres uniformly distributed over the tree top. In the case of the SMOS REFLEX 2003 site, and in order to simplify the geometric and electromagnetic models no clustering effects have been considered. Because of the typical high water content of these components, the number of fruits was determined from the plant volumetric water content (VWC) [kg], the water fraction (WF) [adimensional] of the fruits with respect to the whole plant, and the dry matter fraction (DMF) [adimensional] of the fruits according to:

$$N_{\text{fruits}} = \frac{(\text{VWC} \cdot \text{WF}/d_{\text{w}}) \,/\, (1 - \text{DMF})}{\frac{4}{3\pi R^3}} \tag{A.10}$$

where $d_{\text{w}} = 1.01 \cdot 10^3 \; kg/m^3$, is the water density and R is the radius of the sphere modelling each single fruit.

A.3 Electromagnetic description of the scenario

In order to give the maximum flexibility to EMISVEG, several scattering methods were implemented covering the different shapes and dimensions of the elements in the scenario.

A.3.1 Soil surface

At horizontal and vertical polarisations the soil emission was estimated using the Wang & Choudhury [1981] model. The Kirchhoff model [Tsang *et al.*, 2000, pp. 925–942] was also implemented in the simulator, with correlation lengths $l = l_x = l_y$. These coefficients, once integrated over the upper hemisphere, provide the full-polarimetric emissivity vector of the soil. In both cases, since the correlation length is the same in both directions, for a horizontal soil the third and fourth elements of the Stokes vector are equal to zero. The effect of the soil moisture content is introduced in the model through the simple dielectric constant model [Wang & Schmugge, 1980].

A.3.2 Trunks, branches and stems

Two methods were implemented for the computation of the scattering by trunks, branches and stems: the semi-exact solution [Ulaby & Elachi, 1990], and the physical optics solution for multi-layer finite length cylinders with corrugation [Lin & Sarabandi, 1995].

A.3.3 Leaves and fruits

The scattering by leaves was computed using the Rayleigh-Gans approximation [Ulaby & Elachi, 1990] for ellipsoids in its different particularisations for flat ellipses, flat discs and needles. Grapes were modelled as dielectric spheres, so the Mie scattering formulation of a group of randomly distributed spherical scatterers was implemented [Tsang *et al.*, 2000, pp. 352-362].

Appendix B

List of Publications

B.1 Book chapters

1. **A. Monerris**, M. Vall-llossera, and A. Camps, "Soil moisture monitoring using L-band radiometry", submitted for publication in *Geoscience and Remote Sensing Book* by InTech, 2009

B.2 Journals

2. **A. Monerris**, P. Benedicto, M. Vall-llossera, A. Camps, E. Santanach, M. Piles, and R. Prehn, "Assessment of the topography impact on microwave radiometry at L-band", *J. Geophys. Res.*, 113, B12202, doi:10.1029/2008JB005602.

3. M. Talone, A. Camps, **A. Monerris**, M. Vall-llossera, P. Ferrazzoli, and M. Piles, "Surface topography and mixed pixel effects on the simulated L-band brightness temperatures", *IEEE Transactions on Geoscience and Remote Sensing*, vol. 45, pp. 1996–2003, July 2007.

4. M. Vall-llossera, A. Camps, I. Corbella, F. Torres, N. Duffo, **A. Monerris**, R. Sabia, D. Selva, C. Antolín, E. López-Baeza, J.F. Ferrer, and K. Saleh, "SMOS REFLEX 2003: L-band emissivity characterization of vineyards", *IEEE Transactions on Geoscience and Remote Sensing*, vol. 43, no. 5, pp. 973–982, May 2005.

5. A. Camps, M. Vall-llossera, R. Villarino, N. Reul, B. Chapron, I. Corbella, N. Duffo, F. Torres, J. Miranda, R. Sabia, **A. Monerris**, and R. Rodríguez, "The emissivity of foam-covered water surface at L-band: theoretical modeling and experimental results from the FROG 2003 field experiment", *IEEE Transactions on Geoscience and Remote Sensing*, vol. 43, no. 5, pp. 925–937, May 2005.

6. R. Sabia, A. Camps, M. Vall-llossera, R. Villarino, J. Miranda, **A. Monerris**, and M. Zapata, "Sea surface salinity retrieval within the ESA Soil Moisture and Ocean Salinity (SMOS) mission", *Atti della Fondazione Giorgio Ronchi*.

7. A. Martínez-Vázquez, A. Camps, J.M. López-Sánchez, M. Vall-llossera, and **A. Monerris**,"Numerical simulations of the full-polarimetric emissivity of vines and comparison with the SMOS REFLEX 2003 experimental data", submitted for publication in Radio Sci., 2009.

8. **A. Monerris**, M. Vall-llossera, A. Camps, M. Cardona, and R. Sabia, "Soil texture effects on soil emission at L-band", submitted as an invited paper to CMDPI, 2009.

B.3 Conferences

9. C. Pérez-Gutiérrez, N. Sánchez-Martín, J. Martínez-Fernández, G. Baroncini-Turricchia, J. Álvarez- Mozos, M. Vall-llossera, A. Aguasca, A. Camps, **A. Monerris**, N. Rodríguez-Álvarez, M. Piles, R. Acevo. "Determinación de parámetros de rugosidad y vegetación in situ para la estimación de la humedad del suelo: El experimento GRAJO(GPS and Radiometric Joint Observations)". *Congreso de la Asociación Española de Teledetección*, Calatayud (Spain), September 2009.

10. F. Torres and **A. Monerris**. "CP34: A Spanish infrastructure to provide global salinity and soil moisture maps from SMOS satellite observations", *OceanObs*, Venezia (Italy), September 2009.

11. **A. Monerris**, N. Rodríguez-Alvarez, M. Vall-llossera, A. Camps, M. Piles, J. Martínez-Fernández, N. Sanchez-Martín, C. Pérez-Gutiérrez, G. Baroncini-Turricchia, R. Acevo, and A. Aguasca."The GPS and Radiometric Joint Observations Experiment at the REMEDHUS Site (Zamora-Salamanca Region, Spain)", *International Geoscience and Remote Sensing Symposium*, Cape Town (South Africa), July 2009.

12. N. Rodríguez-Alvarez, **A. Monerris**, X. Bosch-Lluis, A. Camps, J.F. Marchán-Hernández, I. Ramos-Pérez, E. Valencia, M. Vall-llossera, and J.M. Nieto. "Soil moisture retrieval using GNSS-R: Vegetation effects", *International Geoscience and Remote Sensing Symposium*, Cape Town (South Africa), July 2009.

13. **A. Monerris**, A. Camps, M. Vall-llosera, and M. Piles. "Rock fraction effect on the surface soil moisture estimates from L-band radiometric measurements", *in Proc. International Geoscience and Remote Sensing Symposium*, Boston (USA), July 2008.

14. **A. Monerris**, A. Camps, M. Vall-llosera, E. Santanach and P. Benedicto. "L-band radiometric observations of Sun-glint over land surfaces", *in Proc. International Geoscience and Remote Sensing Symposium*, Boston (USA), July 2008.

15. E. Angiuli, **A. Monerris**, and F. Del Frate. "Application of neural networks to soil moisture retrievals from L-band radiometric data", *in Proc. International Geoscience and Remote Sensing Symposium*, Boston (USA), July 2008.

16. **A. Monerris**, M. Vall-llossera, A. Camps, and M. Piles, "Radiometric observations of vines from the green period to the withering", *in Proc. 10th Specialist Meeting on Microwave Radiometry and Remote Sensing Applications*, 11–14 March, Firenze (Italy), 2006.

17. **A. Monerris**, A. Camps, and M. Vall-llossera, "Empirical determination of the soil emissivity at L-band: Effects of soil moisture, soil roughness, vine canopy, and topography", *in Proc. International Geoscience and Remote Sensing Symposium*, (CD-ROM), 23–27 July, Barcelona (Spain), 2007.

18. **A. Monerris**, P. Benedicto, M. Vall-llossera, A. Camps, M. Piles, E. Santanach, and R. Prehn, "Topography effects on the L-band emissivity of soils: TuRTLE 2006 field experiment", *in Proc. International Geoscience and Remote Sensing Symposium*, (CD-ROM), 23–27 July, Barcelona (Spain), 2007.

19. M. Piles, A. Camps, M. Vall-llossera, **A. Monerris**, M. Talone, and J.L. Álvarez-Pérez, "Deconvolution algorithms in image reconstruction for aperture synthesis radiometers", *in Proc. International Geoscience and Remote Sensing Symposium*, (CD-ROM), 23–27 July, Barcelona (Spain), 2007.

20. **A. Monerris**, M. Vall-llossera, A. Camps, R. Sabia, A. Martínez-Vázquez, I. Ledesma, and M. Piles, "Field experiments to improve the Soil emission models at L-band: Contribution of the UPC to the ESA SMOS mission", *in Proc. Recent Advances in Quantitative Remote Sensing*, 25–29 September, Torrent (Spain), 2006.

21. **A. Monerris**, E. Santanach, M. Vall-llossera, A. Camps, M. Cardona, C. Cantero, and M. Piles, "Roughness effects on the L-band emission of bare soils: The T-REX field experiment", *in Proc. International Geoscience and Remote Sensing Symposium*, (CD-ROM), 31 July–4 August, Denver (USA), 2006.

22. M. Talone, A. Camps, **A. Monerris**, M. Vall-llossera, M. Piles, and P. Ferrazzoli, "Surface topography and mixed pixel effects on the simulated L-band brightness temperatures", *in Proc. 9th Specialist Meeting on Microwave Radiometry and Remote Sensing Applications*, pp. 181–186, 22–24 February, San Juan (Puerto Rico), 2006.

23. **A. Monerris**, M. Vall-llossera, A. Camps, R. Sabia, R. Villarino, M. Cardona, E. Alvarez, and S. Sosa, "Soil moisture retrieval using L-band radiometry: Dependence on soil type and moisture profiles", *in Proc. 9th Specialist Meeting on Microwave Radiometry and Remote Sensing Applications*, pp. 171–175, 22–24 February, San Juan (Puerto Rico), 2006.

24. M. Cardona, M. Vall-llossera, S. Blanch, A. Camps, and **A. Monerris**, "L-Band dielectric properties of different soil types collected during the MOUSE 2004 field experiment", *in Proc. International Geoscience and Remote Sensing Symposium*, (CD-ROM), 25–29 July, Seoul (Korea), 2005.

25. **A. Monerris**, M. Cardona, M. Vall-llossera, A. Camps, R. Sabia, R. Villarino, E. Álvarez, and S. Sosa, "Soil Moisture Retrieval errors using L-band radiometry induced by the soil type variability", *in Proc. International Geoscience and Remote Sensing Symposium*, (CD-ROM), 25–29 July, Seoul (Korea), 2005.

26. M. Vall-llossera, A. Camps, **A. Monerris**, E. Lopez-Baeza, and C. Antolín, "Obtención de la humedad del suelo mediante medidas radiométricas en banda L. Efectos de la rugosidad, tipo de terreno y vegetación", *in Proc. XI Congreso Nacional de Teledetección*, 21–23 September, Tenerife (Spain), 2005.

27. R. Villarino, A. Camps, M. Vall-llossera, J. Miranda, R. Sabia, **A. Monerris**, R. Rodríguez, F. Campoy, J. Fernández, I. Corbella, N. Duffo, F. Torres, and J. Arenas, "Sea surface emission at L-band results from the WISE/FROG field experiments", *in Proc. International Geoscience and Remote Sensing Symposium*, (CD-ROM), 20–24 September, Anchorage (Alaska, USA), 2004.

28. R. Sabia, A. Camps, M. Vall-llossera, R. Villarino, J. Miranda, **A.Monerris**, and M. Zapata, "Sea surface salinity retrieval within the ESA Soil Moisture and Ocean Salinity (SMOS) mission", *in Proc. IEEE GOLD Remote Sensing Conference*, 13 and 14 May, Napoli (Italy), 2004.

29. M. Vall-llossera, A. Camps, I. Corbella, F. Torres, N. Duffo, **A. Monerris**, R. Sabia, D. Selva, C. Antolín, E. López-Baeza, F. Ferrer, and K. Saleh, "SMOS REFLEX 2003: L-band radiometric characterization of vineyards", *in Proc. 8th Specialist Meeting on Microwave Radiometry and Remote Sensing Applications*, 24–27 February, Roma (Italy), 2004.

30. A. Camps, M. Vall-llossera, R. Villarino, I. Corbella, N. Duffo, F. Torres, R. Rodríguez, R. Sabia, **A. Monerris**, I. Corbella, N. Duffo, and F. Torres, "Foam-covered and rain-roughned sea surface emissivity at L-band results from the FROG 2003 experiment", *in Proc. 8th Specialist Meeting on Microwave Radiometry and Remote Sensing Applications*, 24–27 February, Roma (Italy), 2004.

31. M. Vall-llossera, A. Camps, E. López-Baeza, C. Antolín, **A. Monerris**, R. Sabia, D. Selva, J.F. Ferrer, and K. Saleh, "SMOS REFLEX 2003: Preliminary results of soil moisture dependence of the L-band brightness temperature of vineyards measured with the LAURA radiometer", *in Proc. 1st NATO-CCMS and Science Committee Workshop on Desertification in the Mediterranean Region*, 2–5 December, Valencia (Spain), 2003.

32. **A.Monerris**, A. Camps, and M.Vall-llossera, "Study of Multi-angular soil moisture retrieval algorithms on L-band. Application to ESA's SMOS mission", *in Proc. SPIE International Symposium on Remote Sensing*, Barcelona (Spain), 8–12 September, 2003.

B.4 Workshops

33. **A. Monerris**, N. Rodríguez-Álvarez, A. Camps, M. Vall-llosera, and M. Piles. "Overview of UPC experiments over land surfaces". *International Workshop on Microwave Remote Sensing for Land Hydrology Research and Applicatons*, Oxnard (CA, USA), October 2008.

34. M. Piles, A. Camps, M. Vall-llosera, **A. Monerris**, J. Martínez-Fernández, N. Sánchez-Martín, C. Pérez-Gutiérrez, and G. Baroncini-Turricchia. "Calibration and validation of SMOS-derived soil moisture data in the central part of the Duero basin: Experimental activities". *International Workshop on Microwave Remote Sensing for Land Hydrology Research and Applicatons*, Oxnard (CA, USA), October 2008.

35. A. Camps, M. Talone, M. Vall-llossera, **A. Monerris**, P. Ferrazzoli, I. Corbella, N. Duffo, and F. Torres, "The SMOS End-to-End Performance Simulator(SEPS): Recent Improvements in Support to the SMOS CAL/VAL", *7th SMOS Workshop*, ESA-ESRIN, Frascati (Italy), 29–31 October, 2007.

Appendix C

List of Symbols

A_r Effective area of the antenna

A_s Area of soil

A_t Total radiating area

b b-factor used to estimate the vegetation optical thickness

$B(\theta,\phi)$ Brightness

B_{bb} Brightness of a black body

$B_f(\theta,\phi)$ Spectral brightness density

C Soil clay fraction

C_s Coefficient which intervenes in the estimation of the soil effective temperature

c Speed of light, $3{\cdot}10^8$ [m/s]

c_s Equivalent soil depth filled with solid

D_s Total equivalent density of the soil made up of solids, water, and air

$e(\theta,\phi)$ Emissivity

e_bs Emissivity of a bare soil

$e_s(\theta,\phi)$ Soil emissivity

$E(z,t)$ Plane wave electric field

f Frequency [Hz]

$F_n(\theta,\phi)$ Normalised antenna pattern

$F_t(\theta,\phi)$ Antenna radiation pattern

FC Field capacity

G Radiometer gain

h Planck constant, $6.63{\cdot}10^{-34}$ [Js]

h_s Effective roughness parameter

$h_\text{air-soil}$ Transition layer thickness used to evaluate the small-scale soil roughness (m)

k Boltzmann constant, $1.38{\cdot}10^{-23}$ [J/K]

$\hat{k}$ Direction vector from the radiometer to the observed pixel

k_λ Electromagnetic wave number

L_a Atmospheric attenuation

l_c Correlation length of the soil roughness profile

L_veg Attenuation due to a vegetation canopy

n Exponential of the cosine dependence of soil emissivity with the incidence angle

p Polarisation (vertical or horizontal)

P Power collected by an antenna

P_n^ini First-guess value of the parameter P_n

P_bb Power collected by an antenna

P_s Soil porosity

Q_s Cross-polarisation factor

R Distance between the antenna and the radiating target

R_h Fresnel reflectivity of soils at horizontal polarisation

R_v Fresnel reflectivity of soils at vertical polarisation

S Soil sand fraction

T Absolute physical temperature [K]

T_{AP} Absolute temperature [K]

T_{UP} Atmospheric upward radiation [K]

T_{SC} Radiation scattered by the land surface [K]

T_{DN} Atmospheric downward radiation reflected by the surface [K]

T_B Brightness temperature [K]

T_{Bh} Brightness temperature at horizontal polarisation [K]

T_{Bv} Brightness temperature at vertical polarisation [K]

T_{Bp}^{model} Simulated brightness temperature at p polarisation (p is either vertical or horizontal) [K]

T_{eff} Effective soil temperature [K]

T_h First Stokes parameter in brightness temperature [K]

T_N Noise temperature [K]

T_{soil} Soil surface physical temperature [K]

T_{surf} Soil surface temperature [K]

T_v Second Stokes parameter in brightness temperature [K]

T_{veg} Vegetation physical temperature [K]

T_∞ Deep soil temperature [K]

U Third Stokes parameter in brightness temperature [K]

V Fourth Stokes parameter in brightness temperature [K]

VWC Vegetation water content [kg/m^2]

V_{a} Volume fraction of air in soils

V_{bw} Volume fraction of bound water in soils

V_{fw} Volume fraction of free water in soils

V_s Volume of a soil sample [cm^3]

V_{sp} Volume fraction of solid phase in soils

V_{out} Output voltage of a radiometer [V]

V_w Volume of water in a soil sample [cm^3]

w_d Dry weights of a soil sample [g]

w_g Gravimetric soil moisture

w_s Volumetric soil water content [m^3/m^3]

w_t Transition moisture [m^3/m^3]

WP Wilting point [m^3/m^3]

w_w Wet weight of a soil sample [g]

α Exponential of the soil dielectric mixing model

Δf Bandwidth of the receiver

ΔT Radiometric sensitivity

ε_s Soil dielectric constant

ε_s' Real part of the soil dielectric constant

ε_s'' Imaginary part of the soil dielectric constant

ε_{a} Dielectric constant of air in soils

$\varepsilon_{\mathrm{bw}}$ Dielectric constant of bound water in soils

$\varepsilon_{\mathrm{fw}}$ Dielectric constant of free water in soils

ε_{i} Dielectric constant of ice

ε_{r} Dielectric constant of rocks

$\varepsilon_{\mathrm{sp}}$ Dielectric constant of solid phase in soils

ε_{x} Dielectric constant of the initially adsorbed water in soils

$\varepsilon_{\mathrm{w}\infty}$ High frequency limit of $\varepsilon_{\mathrm{fw}} \approx 4.9$

$\varepsilon_{\mathrm{w}0}$ Static dielectric constant of water

ε_0 Permittivity of free space, $8.854{\cdot}10^{-12}$ [F/m]

λ Wavelength [m]

Γ_s Soil reflectivity

Γ_{op} Fresnel's soil reflectivity at p-polarisation

τ Vegetation opacity [Np]

τ_o First guess of the vegetation opacity [Np]

τ_{r} Integration time of a radiometer [s]

τ_{w} Relaxation time of water [s]

ω Vegetation albedo

ω_o First guess of the vegetation albedo

Ω_t Solid angle of the transmitting antenna

φ Azimuth angle referred to nadir[degrees]

φ_A Antenna azimuth angle referred to nadir[degrees]

θ Incidence angle referred to nadir [degrees]

θ_A Antenna incidence angle referred to nadir [degrees]

θ_{local} Pixel's local incidence angle referred to nadir [degrees]

ρ_b Bulk density of soil [g/cm^3]

ρ_w Density of water [g/cm^3]

ρ_{ws} Density of wet soil [g/cm^3]

ρ_p Soil particle density [g/cm^3]

σ_λ Standard deviation of height assuming a windowing of length λ

σ_s Standard deviation of the soil height profile

σ_{pp} Co-polar term of the scattering

σ_{pp} Cross-polar term of the scattering

σ_{P_n} Standard deviation of the parameter P_n

σ_{T_B} Standard deviation of the brightness temperature

σ_τ Standard deviation of the vegetation opacity

σ_ω Standard deviation of the vegetation albedo

Appendix D

List of Acronyms

AMIRAS Airbone Microwave Imaging Radiometer by Aperture Synthesis

AMRS-E Advanced Microwave Scanning Radiometer - E

CASA Construcciones Aeronáuticas Sociedad Anónima

CESBIO Centre d'Etudes Spatiales de la Biosphère

CIDE Centro de Investigaciones sobre la DEsertificación

CNES Centre National d'Etudes Spatiales

CLASIC Cloud LAndSurface Interaction Campaign

CoSMOS Campaign for validating the operation of SMOS

CSIC Consejo Superior de Investigaciones Científicas

DC Direct Current

DoY Day of Year

EEOL End of the Extended Operational Lifetime

ESA European Space Agency

ESTAR Electronically Scanned Thinned Array Radiometer

FC Field Capacity

FROG Foam, Rain, Oil slick, and GPS experiment

FOV Field Of View

GRAJO GPS and RAdiometric Joint Observations experiment

GSFC NASA Goddard Space Flight Center

GPS Global Positioning System

IEEC Institut d'Estudis Espacials de Catalunya

IFAC Istituto di Fisica Applicata "Nello Carrara"

IR Infrared

IROE Istituto di Ricerca sulle Onde Elettromagnetiche "Nello Carrara"

IRTA Institut de Recerca i Tecnologia Agroalimentàries

ISU Iowa State University

JRC Joint Research Centre

LAI Leaf Area Index

LAURA L-band AUtomatic RAdiometer

LCD Liquid Crystal Display

LEWIS L-band radiometer for Estimating Water In Soils

LICEF Light Cost Effective Front-end, SMOS antennæ

MBE Mean Beam Efficiency

MELBEX SMOS Mediterranean Ecosystem L-Band characterisation EXperiment

MIRAS Microwave Imaging Radiometer by Aperture Synthesis

MOUSE MOnitoring Underground Soil Experiment

NASA National Aeronautics and Space Administration

NIR Noise Injection Radiometer

ONERA Office National d'Etudes et de Recherches Aerospatiales

PALS Passive/Active L/S band radiometer

RSLab Remote Sensing Laboratory

REFLEX REFerence pixel L-band EXperiment

RMSE Root Mean Squared Error

SGP Southern Great Plains experiment

SM Soil Moisture

SMAP Soil Moisture Active and Passive

SMEX Soil Moisture EXperiments

SMOS Soil Moisture and Ocean Salinity

SMOSREX Surface Monitoring Of the Soil Reservoir EXperiment

STARSS Salinity Temperature and Roughness Remote Scanner

TDR Time Domain Reflectometry probe

TPR Total Power Radiometer

T-REX Terrain-Roughness EXperiment

TUD Technical University of Denmark

TuRTLE Topography effects on RadiomeTry at L-band Experiment

UdL Universitat de Lleida

UPC Universitat Politècnica de Catalunya

UPS Uninterruptible Power Supply

USDA United States Department of Agriculture

UTV Università degli Studi di Roma Tor Vergata

UV Universitat de València

VAS Valencia Anchor Station

VWC Vegetation Water Content

WISE WInd and Salinity Experiment

WP Wilting Point

List of Figures

List of Tables

Index

Bibliography

Radio Solar Telescope Network (RSTN) data. [Online] Available at: www.ngdc.noaa.gov/stp/SOLAR/ftpsolarradio.html. 9.1.1, 9.1, D

Barré, H.M.J.P., Duesmann, B., & Kerr, Y. 2008. SMOS: The mission and the system. *IEEE Trans. Geosci. and Remote Sens.*, **46**(3), 587–593. 1.2.1, 8.1

Behari, Jitendra. 2005. *Microwave Dielectric Behavior of Wet Soils.* Remote Sensing and Digital Image Processing. Springer. 3.1, 3.2

Benedicto, P. 2007 (November). *Emisividad del terreno en banda L: Estudio del efecto de la topografía y diseño de un radiómetro aerotransportado.* M.Phil. thesis, Universitat Politècnica de Catalunya. 8.1

Berger, M., López-Baeza, E., Wigneron, J.-P., Calvet, J.-C., Simmonds, L., Miller, J., Finkenzeller, H., Etcheto, J., Camps, A., Font, J., Wursteisen, P., Main, B., Fletcher, P., Kerr, Y., & Attema, E. 2002 (24-28 June). The EuroSTARRS campaign in support of the Soil Moisture and Ocean Salinity mission. *Pages 1152–1154 of: Proc. IGARSS*, vol. 2. 1.3.2, 4.8, 8.1

Bindlish, R., Jackson, T.J., Gasiewski, A.J., Klein, M., & Njoku, E. 2006. Soil moisture mapping and AMSR-E validation using the PSR in SMEX02. *Remote Sens. Environ.*, **103**, 127–139. 1.3.3

Bindlish, R., Jackson, T.J., Gasiewski, A., Stankov, B., Klein, M., Cosh, M.H., Mladenova, I., Watts, C., Vivoni, E., Lakshmi, V., Bolten, J., & Keefer, T. 2008. Aircraft based soil moisture retrievals under mixed vegetation and topographic conditions. *Remote Sens. Environ.*, **112**, 375–390. 1.3.3, 7.1

Birchak, J.R., Gardner, C.G., Hipp, J.E., & Victor, J.M. 1974. High dielectric constant microwave probes for sensing soil moisture. *Pages 92–98 of: Proc. IEEE*, vol. 62. 3.2, 3.2.2

Blanch, S., & Aguasca, A. 2004. Seawater dielectric permittivity model from measurements at L-band. *Pages 1362–1365 of: in Proc. IGARSS*, vol. 2. 5.2.1, 5.7

Bosch-Lluís, X., Camps, A., Marchán-Hernández, J.F., Ramos-Pérez, I., Rodríguez-Alvarez, N., Banqué, X., & Guerrero, M. A. 2007. Calibration and performance analysis of the PAU- RAD instrument. *Pages 2419–2422 of:* Camps, A. (ed), *Proc. IEEE IGARSS*. 1.3.1

Brady, N.C., & Weil, R.R. 2003. *Elements of the Nature and Properties of Soils*. 2nd edn. NJ: Prentice Hall. 3.1

Brunfeldt, D. R., & Ulaby, F. T. 1984. Measured microwave emission and scattering in vegetation canopies. *IEEE Trans. Geosci. and Remote Sens.*, **GE-22**(2), 520–524. 3.3

Burke, H-H.K., & Schmugge, T.J. 1982. Effects of varying soil moisture contents and vegetation canopies on microwave emission. *IEEE Trans. Geosci. and Remote Sens.*, **20**(3), 268–274. 7.1

Calvet, J.-C., Wigneron, J.-P., Chanzy, A., Raju, S., & Laguerre, L. 1995. Microwave dielectric properties of a silt-loam at high frequencies. *IEEE Trans. Geosci. and Remote Sens.*, **33**, 634–642. 3.2

Camps, A. 1996 (November). *Application of interferometric radiometry to Earth observation*. Ph.D. thesis, Universitat Politècnica de Catalunya. 2.3.2

Camps, A., Corbella, I., Vall-llossera, M., Villarino, R., Enrique, L., Font, J., Julià, A., Gabarró, C., Etcheto, J., Boutin, J., Weill, A., Torres, F., Duffo, N., Niclós, R., Caselles, V., Wursteinsen, P., & Martín-Neira, M. 2001 (July). Sea Surface Emissivity Observations at L-band: First Preliminary Results of the Wind and Salinity Experiment WISE 2000. *Pages 1371–1373 of:* IEEE (ed), *Proc. IGARSS*, vol. 3. 4.1

Camps, A., Font, J., Vall-llossera, M., Gabarro, C., Corbella, I., Duffo, N., Torres, F., Blanch, S., Aguasca, A., Villarino, R., Enrique, L., Miranda, J.J., Arenas, J.J., Julia, A., Etcheto, J., Caselles, V., Weill, A., Boutin, J., Contardo, S., Niclós, R., Rivas, R., Reising, S.C., Wursteisen, P., Berger, M., & Martin-Neira, M. 2004. The WISE 2000 and 2001 field experiments in support of the SMOS mission: sea surface L-band brightness temperature observations and their application to sea surface salinity retrieval. *IEEE Trans. Geosci. and Remote Sens.*, **42**(4), 804–823. 4.1, 4.8.1, 5.6.1, 8.3.6, 9.1

Camps, A., Vall-llossera, M., Villarino, R., Reul, N., Chapron, B., Corbella, I., Duffo, N., Torres, F., Miranda, J.J., Sabia, R., Monerris, A., & Rodríguez, R. 2005a. The emissivity of foam-covered water surface at L-band: theoretical modeling and experimental results from the FROG 2003 field experiment. *IEEE Trans. Geosci. and Remote Sens.*, **43**(5), 925–937. 4.1, 9.1.4

Camps, A., Vall-llossera, M., Reul, N., Torres, F., Duffo, N., & Corbella, I. 2005b (July). Impact and Compensation of Diffuse Sun Scattering in 2D Aperture Synthesis Radiometers Imagery. *Pages 4906–4909 of: Proc. IGARSS*, vol. 7. 9.1

Camps, A., Bosch-Lluís, X., Ramos-Pérez, I., Marchán-Hernández, J.F., Izquierdo, B., & Rodríguez-Alvarez, N. 2007. New Instrument Concepts for Ocean Sensing: Analysis of the PAU-Radiometer. *IEEE Trans. Geosci. and Remote Sens.*, **45**(10), 3180–3192. 1.3.1

Cano, A., Wigneron, J.-P., Millán-Scheiding, C., Antolín, C., Balling, J., Grant, J., Kruszewski, A., Saleh, K., Søbjaerg, S., Skou, N., & López-Baeza, E. 2007 (July). The SMOS Mediterranean Ecosystem L-band characterisation EXperiment (MELBEX) over natural shrubs. *In: Proc. IGARSS*. 1.3.2, 7.1

Cano, A., Millán-Scheiding, C., Wigneron, J.-P., Antolín, C., Balling, J., Grant, J., Kruszewski, A., Saleh, K., Søbjaerg, S., Skou, N., & López-Baeza, E. 2008 (March). The Mediterranean Ecosystem L-Band EXperiment over vineyards (MELBEX-II). *In: Proc. MicroRad*. 1.3.2

Cardona, M. 2005. *Análisis del efecto de la rugosidad y la permitividad en la emisividad en la emisividad en banda L.* M.Phil. thesis, Universitat Politècnica de Catalunya. 5.2.1

Chanzy, A., Raju, S., & Wigneron, J.-P. 1997. Estimation of soil microwave effective temperature at L and C bands. *IEEE Trans. Geosci. and Remote Sens.*, **35**(3), 570–580. 3.3.4

Choudhury, B.J., Schmugge, T.J., Chang, A.T.C., & Newton, R.W. 1979. Effect of surface roughness on the microwave emission of soils. *Journal of Geophysical Research*, **84**, 5699–5705. 3.3.2, 3.3.2, 6.14, D

Choudhury, B.J., Schmugge, T.J., & Mo, T. 1982. A simple parameterization of effective soil temperature for microwave emission. *J. Geophys. Res.*, 1301–1304. 3.3, 3.3.4, 7.3.1, 7.4, D

Chukhlantsev, A.A. 2006. *Microwave radiometry of vegetation canopies*. Vol. Advances in Global Change Research. Springer. 3.1.2, 3.2, 3.3.3

Claassen, J., & Fung, A. 1974. The recovery of polarized apparent temperature distributions of flat scenes from antenna temperature measurements. *IEEE Trans. Antennas and Propagation*, **22**(3), 433–442. 8.3.4

Coret, L., Kerr, Y., & Richaume, P. 2006. *Flagging the Topographic Impact on the SMOS Signal*. Tech. rept. SO-TNCBSA-GS-0012, Issue 1.b. CESBIO. 8.1

CREAF. 2006. *Land Cover Map of Catalonia by Centre de Recerca Ecològia i Aplicacions Forestals*. 8.3

Curtis, J.O. 2001. Moisture effect on the dielectric properties of soils. *IEEE Trans. Geosci. and Remote Sens.*, **39**, 125–128. 3.2

de Catalunya, Institut Cartogràfic. 2004. *Digital elevation model of Catalonia, 30 m resolution*. 8.3, 8.3.1

de Griend, A. A. Van, & Wigneron, J.-P. 2004. The b-factor as a function of frequency and canopy type at H-polarization. *IEEE Trans. Geosci. and Remote Sens.*, **42**(4), 786–794. 7.1

De Jeu, R., Holmes, T., & Owe, M. 2004 (February). Deriving land surface parameters from three different vegetated sites with the ELBARA 1.4 GHz passive microwave radiometer. *Pages 434–443 of:* Owe, M., D'Urso, G., Moreno, J. F., & Calera, A. (eds), *Proc. SPIE*. Remote Sensing for Agriculture, Ecosystems, and Hydrology V, vol. 5232. 1.3.2

de Jeu, R., Heusinkveld, B., Vugts, H., Holmes, T., & Owe, M. 2004 (February). Remote sensing techniques to measure dew: The detection of canopy water with an L-band passive microwave radiometer and a spectral reflectance sensor. *Pages 225–235 of: Proc. SPIE*, vol. 5568. 9.2

De Roo, R.D., Erbas, C., & Hornbuckle, B.K. 2006. The Iowa State University direct sampling L-band digital radiometer. *Pages 70–76 of: Proc. IEEE MicroRad.* 1.3.1

de Rosnay, P., Calvet, J.-C., Y-H-Kerr, Wigneron, J.-P., Lemaître, F., Escorihuela, M.J., *et al.* 2006. SMOSREX: A long term field campaign experiment for soil moisture and land surface processes remote sensing. *Remote Sens. Envirom.*, **102**, 377–389. 1.3.2, 6.2, 7.1

Del Frate, F., & Wang, L. 2001. Sunflower biomass estimation using a scattering model and a neural network algorithm. *Intern. Journal of Remote Sens.*, **22**, 1235–1244. 3.4

Del Frate, F., Ferrazzoli, P., & Schiavon, G. 2003. Retrieving soil moisture and agricultural variables by microwave radiometry using neural networks. *Rem. Sens. Env.*, **84**(2), 174–183. 3.4

Della Vecchia, A., Saleh, K., Ferrazzoli, P., Guerriero, L., & Wigneron, J.-P. 2006. Simulating L-band emission of coniferous forests using a discrete model and a detailed geometrical representation. *IEEE Geosci. and Remote Sens. Letters*, **3**(3), 364–368. 3.3, 3.3.3, 7.1

Dirksen, C., & Dasberg, S. 1993. Improved calibration of time domain reflectometry soil water content measurements. *Soil Sci. Soc. Am. J.*, **57**, 660–667. 5.1.1

Dobson, M. C., Ulaby, F. T., Hallikainen, M. T., & Elrayes, M. A. 1985. Microwave dielectric behaviour of wet soils 2. Dielectric mixing models. *IEEE Trans. Geosci. and Remote Sens.*, **23**, 35–46. 3.2, 3.2.2, 3.2.2, 3.2.2, 4.4, 4.4.4, 5.2.2, 5.7, 5.6.1, 5.6.2, 5.7, 10.1, D

Duffo, N., Torres, F., Corbella, I., González-Gambau, V., Blanch, S., Camps, A., Vall-llossera, M., Alvarez, J.L, Ribo, S., & Martín-Neira, M. 2007 (July). Some results of the MIRAS-SMOS demonstrator campaigns. *Pages 3639–3642 of:* IEEE (ed), *Proc. IGARSS.* 1.2.1

Eagleman, J.R., & Lin, W.C. 1976. Remote sensing of soil moisture by a 21 cm passive radiometer. *J. Geophys. Res.*, **81**, 3660–3666. 1.1

Entekhabi, D., Asrar, G.R., Betts, A.K., Beven, K.J., Bras, R.L., Duffy, C.J., Dunne, T., Koster, R.D., Lettenmaier, D.P., McLaughlin, D.B., Shuttleworth, W.J., van Genuchten, M.T., Wei, M., & Wood, E.F. 1999. An Agenda for Land Surface Hydrology Research and a Call for the Second International Hydrological Decade. *Bulletin of the American Meteorological Society*, **80**(10), 2043–2058. 1.1

Entekhabi, D., Njoku, E., Houser, P., Spencer, M., Doiron, T., Smith, J., Girard, R., Belair, S., Crow, W., Jackson, T., Kerr, Y., Kimball, J., Koster, R., McDonald, K., O'Neill, P., Pultz, T., Runnig, S., Shi, J.C., Wood, E., & van Zyl, J. 2004. The Hydrosphere State (HYDROS) mission concept: An Earth system pathfinder for global mapping of soil moisture and land freeze/thaw. *IEEE Trans. Geosci. and Remote Sens.*, **42**(10), 2184–2195. 1.2.2

ESA. 2003 (July). *Mission objectives and scientific requirements of the SMOS mission*. 1.2.1

Escorihuela, M. J., Kerr, Y. H., de Rosnay, P., Wigneron, J.-P., Calvet, J.-C., & Lemaitre, F. 2007. A simple model of the bare soil microwave emission at L-band. *IEEE Trans. Geosci. and Remote Sens.*, **45**(7), 1978–1987. 1.3.2, 3.3, 3.3.2, 3.3.2, 6.2, 6.2, 6.5.2, 6.10, 6.11, 6.13, 6.14, D

Escorihuela, M.J., Saleh, K., Richaume, P., Merlin, O., Walker, J.P., & Kerr, Y.H. 2008. Sunglint observations over land from ground and airborne L-band radiometer data. *Geophysical Research Letters*, **35**(L20406). 9.1

Escorihuela, M.J., Kerr, Y.H., de Rosnay, P., Saleh, K., Wigneron, J.-P., & Calvet, J.C. 2009. Effects of Dew on the Radiometric Signal of a Grass Field at L-Band. *IEEE Geosci. and Remote Sens. Letters*, **6**(January), 67–71. 7.1, 9.2

Ferrazzoli, P., & Guerriero, L. 1996. Passive microwave remote sensing of forest: A model investigation. *IEEE Trans. Geosci. and Remote Sens.*, **34**, 433–443. 3.3.3

Ferrazzoli, P., Guerriero, L., & Wigneron, J.-P. 2002. Simulating L-band emission of forests in view of future satellite applications. *IEEE Trans. Geosci. and Remote Sens.*, **40**(12), 2700–2708. 3.3, 3.3.3, 6.2, 7.1, 7.3.7

Fetter, C.W. 2001. *Applied hydrogeology*. 4th edn. Prentice Hall. 3.1.3

Fung, A.K. 1994. *Microwave Scattering and Emission. Models and their applications*. Artech House. 3.3.1, 3.3.2, 3.3.2, 5.1.2, 6.2, 6.5.1

Grant, J.P., Wigneron, J.-P., de Griend, A.A. Van, Kruszewski, A., Søbjærg, S., & Skou, N. 2007. A field experiment on microwave forest radiometry: L-band signal behaviour for varying condition of surface wetness. *Remote Sens. Environ.*, **109**(12), 10–19. 1.3.2, 7.1

Hallikainen, M.T., Ulaby, F.T., Dobson, M.C., El-Rayes, M.A., & L-Wu. 1985. Microwave Dielectric Behavior of Wet Soil-Part 1: Empirical Models and Experimental Observations. *IEEE Trans. Geosci. and Remote Sens.*, **GE–23**, 25–34. 3.2, 3.2, D

Hipp, J. E. 1974. Soil electromagnetic parameters as a function of frequency, soil density and soil moisture. *Pages 98–103 of: Proc. IEEE*, vol. 62. 3.2

Holmes, T., de Rosnay, P., de Jeu, R., Wigneron, J.-P., Kerr, Y., Calvet, J.-C., Escorihuela, M. J., Saleh, K., & Lemaître, F. 2006. A new parameterization of the effective temperature for L- band radiometry. *Geophys. Res. Lett.*, **33**, 7405. 3.3, 3.3.4

Hornbuckle, B., England, A., Anderson, M., & Viner, B. 2006. The effect of free water in a maize canopy on microwave emission at 1.4 GHz. *Agric. For. Meteorol.*, **138**(1–4), 180–191. 9.2

Hornbuckle, B.K, & England, A.W. 2004 (July). Radiometric sensitivity to dew at 1.4 GHz relative to soil moisture in a dense canopy. *Pages 439–446 of: Hydrology: science and practice for the 21st century*, vol. 1. 9.2

Hornbuckle, B.K., England, A.W., & Anderson, M. 2007. The effect of intercepted precipitation on the microwave emission of maize at 1.4 GHz. *IEEE Trans. Geosci. and Remote Sens.*, **45**(7), 1988–1995. 9.2

Jackson, T., & Moy, L. 1999. Dew effects on passive microwave observations of land surfaces. *Remote Sens. Environ.*, **36**, 203–212. 9.2

Jackson, T. J., & Schmugge, T. J. 1991. Vegetation effects on the microwave emission from soils. *Remote Sens. Environ.*, **36**, 203–212. 1.1, 3.3, 7.1, 7.4.2, 9.3

Jackson, T. J., Kostov, K. G., & Saatchi, S. S. 1992. Rock fraction effects on the interpretation of microwave emission from soils. *IEEE Trans. Geosci. and Remote Sens.*, **30**(3), 610–616. 7.4.2, 7.4.2

Jackson, T. J., O'Neill, P.E., & Swift, C.T. 1997. Passive microwave observations of diurnal surface soil moisture. *IEEE Trans. Geosci. and Remote Sens.*, **35**, 1210–1222. 7.1

Jackson, T.J., & Schmugge, T.J. 1989. Passive microwave remote sensing system for soil moisture: Some supporting research. *IEEE Trans. Geosci. and Remote Sens.*, **27**(2), 225–235. 1.1

Jackson, T.J., & Schmugge, T.J. 1995. Surface soil moisture measurement with microwave radiometry. *Pages 477–482 of: Acta Astronautica*, vol. 35. Elsevier Science Ltd. 1.1

Jackson, T.J., Schmugge, T.J., & Wang, J.R. 1982. Passive microwave sensing of soil moisture under vegetation canopies. *Water Resources Research*, **18**, 1137–1142. 7.1

Jackson, T.J., Vine, D. M. Le, Hsu, A., Oldack, A., Starks, P., Swift, C., Isham, J., & Haken, M. 1999. Soil moisture mapping at regional scales using microwave radiometry : The Southern Great Plains hydrology experiment. *IEEE Trans. Geosci. and Remote. Sens.*, **37**, 2136–2149. 6.2

Jenny, H. 1994. *Factors of Soil Formation. A System of Quantitative Pedology.* Reprint of the 1941 mcgraw-hill publication edn. NY: Dover Press. 3.1

Kerr, Y., Waldteufel, P., Richaume, P., Davenport, I., Ferrazzoli, P., & Wigeron, J.-P. 2006. *SMOS level 2 processor, Soil moisture algorithm theoretical basis document (ATBD).* v5.a SO-TN-ESL-SM-GS-0001. CESBIO. 9.4

Kerr, Y. H., Waldteufel, P., Wigneron, J. P., Martinuzzi, J. M., Font, J., & Berger, M. 2001. Soil moisture retrieval from space: the Soil Moisture and Ocean Salinity (SMOS) mission. *IEEE Trans. Geosci. and Remote Sens.*, **39**, 1729–1735. 1.2.1

Kerr, Y.H., Font, J., Waldteufel, P., & Berger, M. 2000 (July). *The Soil Moisture and Ocean Salinity Mission - SMOS*. ESA Earth Observation Quarterly. 1.1

Kerr, Y.H., Secherre, F., Lastenet, J., & Wigneron, J.-P. 2003 (21–25 July). SMOS: analysis of perturbing effects over land surfaces. *Pages 908–910 of: Proc. IGARSS*, vol. 2. 8.1

Kirdiashev, K.P., Chukhlantsev, A.A., & Shutko, A.M. 1979. Microwave radiation of the Earth's surface in the presence of vegetation cover. *Radio Eng. Electron. Phys.*, **2**, 37–56. 3.3.3, 7.1

Koster, R.D., Dirmeyer, P.A., Guo, Z., Bonan, G., Chan, E., *et al.* 2004. Regions of Strong Coupling Between Soil Moisture and Precipitation. *Science*, **305**(5687), 1138–1140. 1.1

Krajewski, W.F., Anderson, M.C., Eichinger, W.E., Entekhabi, D., Hornbuckle, B.K., Houser, P.R., Katul, G.G., Kustas, W.P., Norman, J.M., Peters-Lidard, C., & Wood, E.F. 2006. A remote sensing observatory for hydrologic sciences: A genesis for scaling to continental hydrology. *Water Resour. Res.*, **42**. 1.1

Ledesma, I. 2003. *Generación de vegetación mediante L-Systems : Aplicación a la radiometría de microondas*. M.Phil. thesis, Universitat Politècnica de Catalunya. 7.3.7, A

Lemaître, F., Poussière, J.-C., Kerr, Y.H., Déjus, M., Durbe, R., de Rosnay, P., & Calvet, J.-C. 2004. Design and test of the ground-based L-band Radiometer for Estimating Water In Soils (LEWIS). *IEEE Trans. Geosci. and Remote Sens.*, **42**(8), 1666–1676. 1.3.1, 4.1

LeVine, D.M., & Good, J.C. 1983 (August). *Aperture synthesis for microwave radiometry in space*. NASA Technical Memorandum. 2.3.2

LeVine, D.M., Griffis, A.J., Swift, C.T., & Jackson, T.J. 1994 (December). ESTAR: A synthetic aperture microwave radiometer for remote sensing applications. *Pages 1787–1801 of: Proc. of the IEEE*, vol. 82. 1.3.1

Lewis, A. M., & Logreco, A. 2002 (October). *Automatic moisture measurement system for the outdoor test lane*. Technical Note No. I.02.102. Joint Research Centre, Ispra, Italy. 4.4.1, 4.7, 5.1, 5.1.1, D

Lin, Y.C., & Sarabandi, K. 1995. Electromagnetic Scattering Model for a Tree Trunk Above a Tilted Ground Plane. *IEEE Trans. Geosci. and Remote Sens.*, **33**(4), 1063–1070. A.3.2

López-Baeza, E., Antolín, C., Bodas, A., Gimeno, J. F., Saleh, K., Ferrer, F., Castell, N., Doménech, C., Sánchez, M.A., & Velázquez, A. 2001 (September). The Valencia Anchor Station: A reference cal/val area for low-resolution remote sensing data and products. *In: Proc. First International Symposium on Recent Advances in Quantitative Remote Sensing*. 4.6, 4.6.1, 7.2

Macelloni, G., Brogioni, M., Pampaloni, P., Cagnati, A., & Drinkwater, M.R. 2006. DOMEX 2004: An experimental campaign at Dome-C Antarctica for the calibration of spaceborne low-frequency microwave radiometers. *IEEE Trans. Geosci. and Remote Sens.*, **44**(10), 2642–2653. 9.4

Macelloni, G., Pampaloni, P., Pettinato, S., Santi, E., & Drinkwater, M. 2007 (November). The DOMEX-2 experiment : a contribution to SMOS calibration. *In: 7th SMOSWorkshop.* 1.3.1, 9.4

Martínez-Vázquez, A., Camps, A., Duffo, N., Vall-llossera, M., & López-Sánchez, J.M. 2002. Full polarimetric emissivity of vegetation-covered soils: Vegetation structure effects. *In: Proc. IGARSS.* 7.3.7, A, A.2.3

Martínez-Vázquez, A., Camps, A., López-Sánchez, J.M., Vall-llossera, M., & Monerris, A. 2009. Numerical simulations of the full-polarimetric emissivity of vines and comparison with the SMOS REFLEX 2003 experimental data. *submitted for publication.* 7.20, 7.21, 7.22, A, D

Martín-Neira, M., Ribó, S., & Martín-Polegre, A.J. 2002. Polarimetric mode of MIRAS. *IEEE Trans. Geosci. and Remote Sens.*, **40**(8), 1755–1768. 1.2.1

Martín-Neira, M., Cabeza, I., Pérez, C., Palacios, M.A., Guijarro, M.A., Ribó, S., Corbella, I., Blanch, S., Torres, F., Duffo, N., González, V., Beraza, S., Camps, A., Vall-llossera, M., Tauriainen, S., Pihlflyckt, J., González, J.P., & Martín-Porqueras, F. 2008. AMIRAS – An Airborne MIRAS Demonstrator. *IEEE Trans. Geosci. and Remote Sens.*, **46**(3), 705–716. 1.2.1

Mätlzler, C. 1990. Seasonal evolution of microwave radiation from an oat field. *Remote Sensing of Environment*, **31**, 161–173. 7.1

Mätlzler, C., & Standley, A. 2000. Relief effects for passive microwave remote sensing. *J. Geophys. Res.*, **21**, 2403–2412. 3.3, 4.8, 8.1

McMullan, K.D., Brown, M.A., Martín-Neira, M., Rits, W., Martí, J., & Lemanczyk, J. 2008. SMOS: The payload. *IEEE Trans. Geosci. and Remote Sens.*, **46**(3), 594–605. 1.2.1

Merlin, O., Walker, J.P., Kalma, J.D., Kim, E.J., Hacker, J., Panciera, R., Young, R., Summerell, G., Hornbucke, J., Hafeez, M., & Jackson, T.J. 2008. The NAFE'06 data set: towards soil moisture retrieval at intermediate resolution. *Adv. Water Resour.* 1.3.2

Mialon, A., Coret, L., Kerr, Y.H., Sécherre, F., & Wigneron, J.-P. 2008. Flagging the Topographic Impact on the SMOS Signal. *IEEE Trans. Geosci. and Remote Sens.*, **46**(3), 689–694. 8.1

Miller, J.D., & Gaskin, G.J. 1999. *Theta Probe ML2x principles of operation and application.* 2nd edn. Delta-T Devices and MaCaulay Land Use Research Institute. 3.2, 4.2.1, 5.1.1, 5.1.1

Mironov, V.L., Dobson, M.C., Kaupp, V.H., Komarov, S.A., & Kleshchenko, V.N. 2004. Generalized refractive mixing dielectric model for moist soils. *IEEE Trans. Geosci. and Remote Sens.*, **42**(4), 773–785. 3.2

Mo, T., & Schmugge, T.J. 1987. A parameterization ot the effect of surface roughness on microwave emission. *IEEE Trans. Geosci. and Remote Sens.*, **25**, 47–54. 3.3, 3.3.2, 3.3.2, 6.2, 6.2, 6.5.2, 6.10, 6.11, 6.13, 6.14, D

Monerris, A., Santanach, E., Vall-llossera, M., Camps, A., Cardona, M., Cantero, C., & Piles, M. 2006a (July 31 2006-Aug. 4). Roughness Effects on the L-band Emission of Bare Soils: The T-REX Field Experiment. *Pages 1090–1093 of: Proc. IGARSS*. 6.2

Monerris, A., Vall-llossera, M., Camps, A., Sabia, R., Villarino, R., Cardona, M., Alvarez, E., & Sosa, S. 2006b. Soil Moisture Retrieval Using L-band Radiometry: Dependence on Soil Type and Moisture Profiles. *Pages 171–175 of: Proc. MicroRad*. 1, 6.2

Monerris, A., Benedicto, P., Vall-llossera, M., Camps, A., Piles, M., Santanach, E., & Prehn, R. 2007 (July). Topography effects on the L-band emissivity of soils: The TuRTLE 2006 field experiment. *In: Proc. IGARSS*. 4.8

Monerris, A., Benedicto, P., Vall-llossera, M., Santanach, E., Piles, M., & Prehn, R. 2008. Assessment of the topography impact on microwave radiometry at L-band. *Journal of Geophysical Research*, **113**(B12202). 8.1

Mätzler, C. 1994. Passive Microwave Signatures of Landscapes in Winter. *Meteorology and Atmospheric Physics*, **54**, 241–260. 9.4

Mätzler, C., Weber, D., Wuthrich, M., Schneeberger, K., Stamm, C., Wydler, H., & Fluhler, H. 2003. ELBARA, the ETH L-band radiometer for soil-moisture research. *Pages 3058 – 3060 of: Proc. IGARSS*, vol. 5. 1.3.1, 4.1

Mätzler, Christian. 2006. *Thermal Microwave Radiation: Applications for Remote Sensing*. IET Electromagnetic Waves Series 52. 3.3.2, 6.10, 6.11, 6.13, 6.14, D

NASA. 2007. Soil Moisture Active/Passive (SMAP) mission. *In: NASA Workshop Report*. NASA. 1.2.2

Njoku, E., Spencer, M., McDonald, K., Smith, J., Houser, P., Doiron, T., O'Neill, P., Girard, R., & Entekhabi, D. 2004 (March). The HYDROS mission: requirements and system design. *Pages 1000–1007 of: Proc. Aerospace Conference*, vol. 2. 1.2.2

Noborio, K. 2001. Measurement of soil water content and electrical conductivity by time domain reflectometry: a review. *Computers and Electronics in Agriculture*, **31**(3), 213–237. 3.2.1

O'Neill, P.E., Lang, R.H., Kurum, M., Utku, C., & Carver, K.R. 2006. Multi-Sensor Microwave Soil Moisture Remote Sensing: NASA's Combined Radar/Radiometer (ComRAD) System. *Pages 50–54 of: Proc. IEEE MicroRad*. 1.3.1

O'Neill, Peggy, Joseph, Alicia, Nelson, Ross, Cosh, Michael, Jackson, Thomas, Lang, Roger, Kurum, Mehmet, & Spicknall, Mark. 2007 (23–28 July). ComRAD active / passive microwave measurement of tree canopies. *Pages 1420–1423 of: Proc. IGARSS*. 1.3.1

Owe, M., & de Griend, A.A. Van. 1998. Comparison of soil moisture penetration depths for several bare soils at two microwave frequencies and implications for remote sensing. *Water Resources Research*, **34**(9). 5.2.2

Paloscia, S., & Pampaloni, P. 1988. Microwave polarization index for monitoring vegetation growth. *IEEE Trans. Geosci. and Remote Sens.*, **26**(5), 617–621. 7.3.5

Paloscia, S., Pampaloni, P., Chiarantini, L., Coppo, P., Gagliani, S., & Luzi, G. 1993. Multifrequency passive microwave remote sensing of soil moisture and roughness. *Int. J. Remote Sens.*, **14**, 467–483. 6.2

Pardé, M., J.-P.Wigneron, Chanzy, A., P.Waldteufel, Y.Kerr, & Huet, S. 2003. Retrieving surface soil moisture over a wheat field: Comparison of different methods. *Remote Sens. Environ*, **87**, 334–344. 7.1, 7.3.2

Parde, M., Wigneron, J.-P., Waldteufel, P., Kerr, Y.H., Chanzy, A., Sobjaerg, S.S., & Skou, N. 2004. N-parameter retrievals from L-band microwave observations acquired over a variety of crop fields. *IEEE Trans. Geosci. and Remote Sens.*, **42**(6), 1168–1178. 3.4

Peplinsky, N.R., Ulaby, F.T., & Dobson, M.C. 1995. Dielectric properties of soils in the 0.3–1.3 GHz range. *IEEE Trans. Geosci. and Remote Sens.*, **33**, 803–807. Corrections: IEEE Trans. Geosci. and Remote Sens., 1995, 33:1349. 3.2, 3.2.2

Pierdicca, N., Pulvirenti, L., & Marzano, F.S. 2008 (July). A simulation study to quantify the relief effects on the observations performed by microwave radiometers. *Pages 684–687 of: Proc. IGARSS*, vol. II. 8.1

Prusinkiewicz, P., & Lindenmayer, A. 1990. *Algorithmic beauty of plants*. New York: Springer-Verlag. A.2.2

Putuhena, W.M., & Cordery, I. 1996. Estimation of interception capacity of the forest floor. *Journal of Hydrology*, **180**, 283–299. 9.3

Reich, P., & Reich, W. 1986. A radio continuum survey of the northern sky at 1420 MHz - Part II. *Astron. Astrophys. Suppl. Series*, **63**, 205–292. 8.3.5, 9.1.4

Reul, N., Tenerelli, J., Chapron, B., & Waldteufel, P. 2007. Modeling sun glitter at L-band for sea surface salinity remote sensing with SMOS. *IEEE Trans. Geosci. and Remote Sens.*, **45**(7), 2073–2087. 9.1

Robock, A., Vinnikov, K.Y., Srinivasan, G., Entin, J.K., Hollinger, S.E., Speranskaya, N.A., Liu, S., & Namkhai, A. 2000. The global soil moisture data bank. *Bulletin of the American Meteorological Society*, **81**(6), 1281–1299. 1.1

Rodríguez-Alvarez, N., Marchán-Hernández, J.F., Camps, A., Valencia, E., Bosch-Lluis, X., Ramos-Pérez, I., & Nieto, J.M. 2008 (July). Soil Moisture Retrieval Using GNSS-R Techniques: Measurement Campaign in a Wheat Field. *Pages 245–248 of: Proc. IGARSS*, vol. 2. 10.2

Roth, C.H., Malicki, M.A., & Plagge, R. 1992. Empirical evaluation of the relationship between soil dielectric constant and volumetric water content as the basis for calibrating soil moisture measurements by TDR. *J. of Soil Sci.*, **43**, 1–3. 3.2, 3.2, 3.2.2

Rouse, J.W. 1983. Comments on "Effect of texture on microwave emission from soils". *IEEE Trans. Geosci. and Remote Sens.*, **GE-21**(4), 508–510. 5

Saleh, K., Wigneron, J.-P., Ferrazzoli, P., Calvet, J.-C., Lopez-Baeza, E., Mongiardo, G., & Parde, M. 2003 (21-25 July). Monitoring forests from L-band microwave observations. *Pages 1628–1630 of: Proc. IGARSS*, vol. 3. 7.1

Saleh, K., Porte, A., Guyon, D., Ferrazzoli, P., & Wigneron, J.-P. 2005. A Forest Geometric Description of a Maritime Pine Forest Suitable for Discrete Microwave Models. *IEEE Trans. Geosci. and Remote Sens.*, **43**(9), 2024–2035. 7.1

Saleh, K., Wigneron, J.-P., de Rosnay, P., Calvet, J.-C., Escorihuela, M.J., Kerr, Y., & Waldteufel, P. 2006a. Impact of rain interception by vegetation and mulch on the L-band emission of natural grass. *Remote Sens. Environ.*, **101**, 127–139. 3.4, 7.1, 7.4.2, 9.3

Saleh, K., Wigneron, J.-P., de Rosnay, P., Calvet, J.-C., , & Kerr, Y. 2006b. Semi-empirical regressions at L-band applied to surface soil moisture retrievals over grass. *Remote Sens. Environ.*, **101**, 415–426. 9.3

Saleh, K., Wigneron, J.-P., Waldteufel, P., de Rosnay, P., Schwank, M., Calvet, J.-C., & Kerr, Y. 2007a. Estimates of surface soil moisture under grass covers using L-band radiometry. *Remote Sens. Environ.*, **109**, 42–53. 7.1

Saleh, K., Kerr, Y.H., Boulet, G., Maisongrande, P., de Rosnay, P., Floricioiu, D., Escorihuela, M.J., Wigneron, J.-P., Cano, A., López-Baeza, E., Grant, J., Balling, J., Skou, N., Berger, M., Delwart, S., Wursteisen, P., Panciera, R., & Walker, J.P. 2007b (July). The CoSMOS L-Band Experiment in Southeast Australia. *In: Proc. IGARSS*. 1.3.2, 9.3

Schmugge, T.J. 1980. Effect of texture on microwave emission from soils. *IEEE Trans. Geosci. and Remote Sens.*, **GE-18**, 353–361. 5, 5.2.1

Schmugge, T.J., Wang, J.R., & Asrar, G. 1988. Results from the push broom microwave radiometer flights over the Konza Prairie in 1985. *IEEE Trans. Geosci. and Remote Sens.*, **26**, 590–597. 9.3

Schneeberger, K., Schwank, M., Stamm, Ch., de Rosnay, P., Mätzler, Ch., & Flühler, H. 2004. Topsoil Structure Influencing Soil Water Retrieval by Microwave Radiometry. *Vadose Zone Journal*, **3**(November), 1169–1179. 3.3.2, 3.3.2, 6.1.1, 6.2, 6.5.2

Schwank, M., Stähli, M., Wydler, H., Leuenberger, J., Mätzler, C., & Flühler, H. 2004. Microwave L-band emission of freezing soil. *IEEE Trans. Geosci. and Remote Sens.*, **42**(6), 1252–1261. 3.3, 9.4

Shi, J., Chen, K.S., Qin, L., Jackson, T.J., O'Neill, P.E., & Leung, T. 2002. A parameterized surface reflectivity model and estimation of bare-surface soil moisture with L-band radiometer. *IEEE Trans. Geosci. and Remote Sens.*, **40**(12), 2674–2686. 3.3.2, 6.5.2

Shutko, A.M., & Reutov, E.M. 1982. Mixture formulae applied in estimation of dielectric and radiative characteristics of soils and grounds at microwave frequencies. *IEEE Trans. Geosci. and Remote Sens.*, **GE-20**, 29–32. 3.2

Skou, N. 1989. *Microwave radiometer systems: Design and analysis*. Artech House. 2.2.4, 2.3.1, 2.4, D

Søbjærg, S.S. 2002. *Polarimetric Radiometers and their Applications*. Ph.D. thesis, Technical University of Denmark. 1.3.1

Talone, M., Camps, A., Monerris, A., Vall-llossera, M., Ferrazzoli, P., & Piles, M. 2007. Surface topography and mixed pixel effects on the simulated L-band brightness temperatures. *IEEE Trans. Geosci. and Remote Sens.*, **42**(4), 786–794. 3.3, 4.8, 8.1, 8.5, 10.1

Topp, G.C., Davies, J.L., & Annan, A.P. 1980. Electromagnetic determination of soil water content: Measurements in coaxial transmission lines. *Water Resour. Res.*, **16**, 574–582. 3.2, 3.2, 3.2.1, 5.1.1, 5.1.1

Tsang, L., Kong, J.A., & Ding, K. 2000. *Scattering of electromagnetic waves. Theories and applications*. John Wiley & Sons. A.1, A.1, A.1, A.3.1, A.3.3

Ulaby, F. T., Moore, R. K., & Fung, A. K. 1981. *Microwave Remote Sensing: Active and Passive*. Vol. I. Microwave remote sensing fundamentals and radiometry. Reading, Massachusetts: Addison-Wesley. 8.3.5, 8.3.6

Ulaby, F. T., Moore, R. K., & Fung, A. K. 1986. *Microwave Remote Sensing: Active and Passive*. Vol. II, Radar remote sensing and surface scattering and emission theory. Reading, Massachusetts: Addison-Wesley. 2.1, 2.1, 2.2, 2.3, 2.3.1, 3.3.3, 3.3.4, 5.1.2, 6.2, 8.3.5, D

Ulaby, F.T., & Dobson, M.C. 1989. *Handbook of Radar Scattering Statistics for Terrain*. Nordwood MA: Artech House Remote Sensing Library. 9.1.3, 9.1.4

Ulaby, F.T., & Elachi, C. 1990. *Radar polarimetry for geoscience*. Artech House. A.3.2, A.3.3

USDA-ARS. 1997. *Southern Great Plains Experiments*. 1.3.3

Vall-llossera, M., Cardona, M., Blanch, S., Camps, A., Monerris, A., Corbella, I., Torres, F., & Duffo, N. 2005a (July 25–29 July,). L-band dielectric properties of different soil types collected during the MOUSE 2004 field experiment. *Pages 1109–1112 of: Proc. IGARSS*, vol. 2. 4.4.4

Vall-llossera, M., Camps, A., Corbella, I., Torres, F., Duffo, N., Monerris, A., Sabia, R., Selva, D., Antolín, C., López-Baeza, E., Ferrer, J.F., & Saleh, K. 2005b. SMOS REFLEX 2003: L-band emissivity characterization of vineyards. *IEEE Trans. Geosci. and Remote Sens.*, **43**(5), 973–982. 4.6.1

Van de Griend, A. A., & Wigneron, J. P. 2004. The *b*-factor as a function of frequency and canopy type at H-polarization. *IEEE Trans. Geosci. and Remote Sens.*, **42**(4), 786–794. 3.3.3

Villarino, R. 2004 (September). *Empirical Determination of the Sea Surface Emissivity at L-band: A contribution to ESA's SMOS Earth Explorer Mission.* Ph.D. thesis, Remote Sensing Laboratory, Dept. Teoria del Senyal i Comunicacions, Universitat Politècnica de Catalunya. 1.3.1, 2.2.5, 4.1, 4.1, 4.1.1, 8.3.6

Vine, D.M. Le, Abraham, S., Wentz, F., & Lagerloef, G.S.E. 2005. Impact of the sun on remote sensing of sea surface salinty from space. *Proc. IGARSS*, 288–291. 9.1

Walker, J.P., & Panciera, R. 2005. *National Airborne Field Experiment 2005: Experiment Plan.* Tech. rept. Department of Civil and Environmental Engineering,University of Melbourne. 8.1

Wang, J. R., & Schmugge, T. J. 1980. An empirical model for the complex dielectric permittivity of soils as a function of water content. *IEEE Trans. Geosci. and Remote Sens.*, **18**, 288–295. 3.1.7, 3.1.7, 3.2, 3.2.2, 3.2.2, 4.4, 4.4.4, 5.2.2, 5.7, 5.6.1, 5.6.2, 5.7, 8.3.5, 10.1, A.3.1, D

Wang, J.R. 1983. Passive microwave sensng of soil moisture content: The effects of soil bulk densisty and surface roughness. *Remote Sens. Environ.*, **13**, 329–344. 3.3.2, 5, 5.2.1

Wang, J.R., & Choudhury, B.J. 1981. Remote sensing of soil moisture content over bare field at 1.4 GHz frequency. *Journal of Geophysical Research*, **86**, 5277–5282. 1.1, 3.3.2, 3.3.2, 6.2, 6.2, 6.5.2, 6.10, 6.11, 6.13, 6.6, 8.3.5, 9.1.4, 10.1, A.3.1, D

Wang, J.R., McMurtrey, J.E., Engman, E.T., Jackson, T.J., Schmugge, T.J., Gould, W.I., Fuchs, J.E., & Glazar, W.S. 1982. Radiometric measurements over bare and vegetated fields at 1.4 GHz and 5 GHz. *Remote Sens. of Environ.*, **12**, 295–311. 7.1

Wegmüller, U., & Mätzler, C. 1999. Rough bare soil reflectivity model. *IEEE Trans. Geosci. and Remote Sens.*, **37**, 1391–1395. 3.3.2, 6.2

White, I.J., Knight, J.H., Zegelin, S.J., & Topp, G.C. 1994. Comments on "Considerations on the use of time domain reflectometry (TDR) for measuring soil water content". *Eur. J. Soil Sci.*, **45**, 503–508. 5.1.1

Wigneron, J.-P., Kerr, Y.H., Chanzy, A., & Jin, Y.Q. 1993a. Inversion of surface parameters from passive mcirowave measruements over a soybean. *Remote Sens. of Environ.*, **46**, 61–72. 7.1

Wigneron, J.-P., Calvet, J.C., Chanzy, Y. Kerr A., & Lopes, A. 1993b. Microwave emission of vegetation: Sensitivity to leaf characteristics. *IEEE Trans. Geosci. and Remote Sens.*, **31**, 716–726. 7.1

Wigneron, J.-P., Calvet, J.-C., & Kerr, Y. 1996. Monitoring water interception by crop fields from passive microwave observations. *Agricultural and Forest Meteorology*, **80**, 177–194. 9.2, 9.3

Wigneron, J.-P., Laguerre, L., & Kerr, Y.H. 2001. A simple parameterization of the L-band microwave emission from rough agricultural soils. *IEEE Trans. Geosci. and Remote Sens.*, **39**(8), 1697–1707. 3.3, 3.3.2, 3.3.2, 3.3.4, 6.2

Wigneron, J.-P., Calvet, J.-C., Pellarin, T., de Griend, A.A. Van, Berger, M., & Ferrazzoli, P. 2003. Retrieving near-surface soil moisture from microwave radiometric observations: current status and future plans. *Remote Sens. Environ.*, **85**, 489–506. 3.4

Wigneron, J.-P., Parde, M., Waldteufel, P., Chanzy, A., Kerr, Y., Schmidl, S., & Skou, N. 2004. Characterizing the dependence of vegetation model parameters on crop structure, incidence angle, and polarization at L-band. *IEEE Trans. Geosci. and Remote Sens.*, **42**(2), 416–425. 7.1, 7.3.6

Wigneron, J.-P., Chanzy, A., de Rosnay, P., Rüdiger, C., & Calvet, J.-C. 2008. Estimating the effective soil temperature at L-band as a function of soil properties. *IEEE Trans. Geosci. and Remote Sens.*, **46**(3), 797–807. 3.3.4

Wilson, W.J., Yueh, S.H., Dinardo, S.J., Chazanoff, S.L., Kitiyakara, A., Li, F.K., & Rahmat-Samii, Y. 2001. Passive active L- and S-band (PALS) microwave sensor for ocean salinity and soil moisture measurements. *IEEE Trans. Geosci. and Remote Sens.*, **39**(5), 1039–1048. 1.3.1, 4.1

Zhan, X., Houser, P.R., Walker, J.P., & Crow, W.T. 2006. A method for retrieving high-resolution surface soil moisture from HYDROS L-band radiometer and radar observations. *IEEE Trans. Geosci. and Remote Sens.*, **44**(6), 1534–1544. 8.3.5

Zhang, L., Shi, J., Zhang, Z., & Zhao, K. 2003 (July). The estimation of dielectric constant of frozen soil-water mixture at microwave bands. *Pages 2903–2905 of: Proc. IEEE IGARSS*, vol. 4. 9.4

Zundo, M., Barré, H., & Hahne, A. 2005. *SMOS product definition baseline.* SO-TN-ESA-GS-1250. ESA/ESTEC. 1.2.1

Zurita, A. 2008. *Effects of topography on the L-band emission of soils. Analysis of coSMOS-Australia campaign.* ESTEC working paper 2337. European Space Agency. 8.1